Purdue University
Purdue e-Pubs

Open Access Dissertations | Theses and Dissertations

January 2014

Modeling and Validation of S-Drive: A Nestable Piezoelectric Actuator

Aarti Chigullapalli
Purdue University

Follow this and additional works at: https://docs.lib.purdue.edu/open_access_dissertations

Recommended Citation
Chigullapalli, Aarti, "Modeling and Validation of S-Drive: A Nestable Piezoelectric Actuator" (2014). *Open Access Dissertations*. 1501.
https://docs.lib.purdue.edu/open_access_dissertations/1501

This document has been made available through Purdue e-Pubs, a service of the Purdue University Libraries. Please contact epubs@purdue.edu for additional information.

Graduate School ETD Form 9
(Revised /)

PURDUE UNIVERSITY
GRADUATE SCHOOL
Thesis/Dissertation Acceptance

This is to certify that the thesis/dissertation prepared

By Aarti Chigullapalli

Entitled

Modeling and Validation of S-Drive: A Nestable Piezoelectric Actuator

For the degree of Doctor of Philosophy

Is approved by the final examining committee:

Jason V. Clark, Co-Chair

Dimitrios Peroulis, Co-Chair

Jeffrey F. Rhoads

Alina Alexeenko

To the best of my knowledge and as understood by the student in the Thesis/Dissertation Agreement, Publication Delay, and Certification/Disclaimer (Graduate School Form 32), this thesis/dissertation adheres to the provisions of Purdue University's "Policy on Integrity in Research" and the use of copyrighted material.

Approved by Major Professor(s): Jason V. Clark, Co-Chair

Approved by: Ganesh Subbarayan-Shastri 09/04/2014

Head of the Graduate Program Date

MODELING AND VALIDATION OF S-DRIVE:

A NESTABLE PIEZOELECTRIC ACTUATOR

A Dissertation

Submitted to the Faculty

of

Purdue University

by

Aarti Chigullapalli

In Partial Fulfillment of the

Requirements for the Degree

of

Doctor of Philosophy

December 2014

Purdue University

West Lafayette, Indiana

Dedicated to my parents

Venugopal and Nirmala

ACKNOWLEDGEMENTS

I am extremely thankful to my advisors Professor Jason Clark and Professor Dimitrios Peroulis, for giving me this opportunity and supporting me throughout my graduate career. I greatly appreciate Professor Clark for introducing me to this area of research and for all the time he spent in answering my questions. I am grateful for the timely support from Professor Dimitrios Peroulis, for the fabrication and experimental work.

I also would like to thank Professor Alina Alexeenko and Professor Jeffrey Rhoads for providing advice and guidance by serving on my advisory committee. I deeply appreciate the timely advice given by Professor Alexeenko, which helped me in finishing my work. I would like to record my deep sense of gratitude to William E. and Florence E. Perry Head of Mechanical Engineering & Alpha P. Jamison Professor Anil Bajaj, without whom completion of this work would not have been possible.

I am particularly grateful to Michael Sinani and Zhe Luo for helping me with the fabrication and experiments. I have been helped in various ways by my research group mates, Prabhakar Marepalli, Xing Jin, Nathanael Andrews and Ameya Apte.

I am very thankful to Professor Emeritus David Anderson for giving me various teaching opportunities. I would like to thank Professor Ganesh Subbarayan for helping me with the thesis formatting. I would also like to thank Julayne Moser and Cathy Elwell in the office of the School of Mechanical Engineering for their whole-hearted help and eager cooperation.

I would like to thank my high school friends Anvesh, Deepthi, Bharath, Rahul, Satwik, Dheeraj, Neha, Vishal, Prashanthi, Mythree, Abhinand, and Sai Kiran for all their encouragement throughout my graduate studies.

I feel very lucky to have found the best family at Purdue, the Asha Purdue Family (Prasoon, Neha, Gaurav, Romi, Suchismita, Susmita, Pratikash, Kritika), away from my family in India. They were were there to celebrate the happy times and they did not leave my side at tough times. I would like to thank Susmita my friend from day one at Purdue for going through all the milestones at Purdue with me. Pratikash and Susmita thanks for the awesome years at Purdue and all the amazing long weekends. Thanks to my lunch buddy Suchismita without whom lunch on campus would have been boring. Thanks to Prasoon and Neha for taking such good care of me at BeauJardin, I will definitely miss Neha's awesome food and useful discussions with Prasoon. Thanks to Kritika for those long discussions during IR. Thanks to Gaurav, Romi for all the fun filled evenings and for their special addition Aisha (kutty Pradhan) to the Asha family. For the last five months she has been a great stress buster.

I would like to thank my parents Venugopal and Nirmala for the sacrifices they made for helping me achieve my goals in life. Thanks to my sisters Deepti and Sruti who have guided me throughout my life and helped me in becoming a better person. I would

like to thank my role model Deepti for everything she did. I'm extremely thankful to Sruti and Jayender for guiding me throughout my undergraduate studies and helping me join Purdue. Thanks for taking such great care of me and making sure that I never missed home. I would also like to thank my grandfather Lakshminarayana, for all his math classes, intellectual talks and for inspiring me to do a Ph.D. I would like to thank my grandmother Lakshmi, for believing in me and always supporting my decision to take up higher studies. I would also like to thank my nephews Rishith and Nishanth for their extremely cute talks that helped me get through stressful times at Purdue. I would like to thank Usha aunty and Prakash uncle for taking such good care of me in India. I would like to thank Sudhakar mama, Amar mama's family, Sarala pinni's family, Nagisetty peddanana's family, Vidyasagar peddamama's family, Subbamatha's family, Murali peddanana's family and Kumar babai's family for their constant moral support which has been essential for the successful completion of my work.

I also feel very lucky to have gotten engaged to Vinod my best friend forever. I feel blessed to have found such a great person at Purdue. Vinod, thanks for staying by my side during the crucial years of my Ph.D., your constant motivation and moral support helped me with finishing this epic journey. Finally, I would like to thank my future in-laws Radha aunty, Venkatakrishnan uncle and Vaishnavi for all their support and prayers that helped in finishing this work.

TABLE OF CONTENTS

Page

LIST OF TABLES ix
LIST OF FIGURES x
SYMBOLS xvii
ABSTRACT xix
CHAPTER 1. INTRODUCTION 1
1.1 Nestability 1
1.2 Motivation 2
1.3 State of Art 4
1.4 Other 'S' Shaped Actuators 6
1.5 Various Actuation Mechanisms 7
1.6 Previous Efforts of Nestability 8
1.7 Organization of Dissertation 9
CHAPTER 2. THEORY OF PIEZOELECTRICITY 10
2.1 Piezoelectric Mechanism 10
2.2 Piezoelectric Materials 12
2.2.1 Piezoelectric Ceramics (PZT) 13
2.2.2 Polyvinylidene Fluoride (PVDF) 14
2.3 Limits of Operation 15
2.4 Applications of Piezoelectric Materials 17
CHAPTER 3. S-DRIVE A NESTABLE PIEZOELECTRIC ACTUATOR 18
3.1 S-Drive Concept 19
3.2 Finite Element Analysis Modeling of S-drive 19
3.3 Analytical Modeling of S-drive 20
3.3.1 Assumptions 20
3.3.2 Lateral Displacement and Stiffness 22

Page

3.4 Effect of Scaling 27

3.5 Other Possible Designs of S-drive 28

CHAPTER 4. NESTABILITY 30
4.1 1D Array....30

4.1.1 Axial-Mode....31

4.1.2 Shear-Mode 33

4.2 2D Array....34

4.2.1 Axial-Mode....34

4.2.2 Shear-Mode 35

CHAPTER 5. EXPERIMENTAL VALIDATION OF DEVELOPED ANALYTICAL MODEL AND FEA SIMULATIONS....36
5.1 Fabricated S-Drive Design....36

5.2 Simulation 37

5.3 Analytical Model 38

5.4 Fabrication....43

5.5 Experimental Setup....45

5.6 Experimental Results 46

5.7 Time for Charging and Discharging 49

5.8 Measured Displacements while Switching from $+V_0$ to $-V_0$....50

5.9 Microfabrication 50

CHAPTER 6. POSSIBLE APPLICATIONS OF NESTED S-DRIVES....52
6.1 Dip Pen Nanolithography....52

6.1.1 Advantages of DPN 53

6.1.2 Types of DPN 53

6.2 Nested S-Drive Design....55

6.2.1 Pen/Probe Design....55

6.2.2 Electrode Connections 56

6.2.3 One Complete Cycle for In-Plane Movement....57

6.2.4 Out-of-Plane Movement....58

6.2.5 Possible Fabrication Steps....58

6.3 Summary of S-drive Pen/Probe 60

Page

CHAPTER 7. SUMMARY AND FUTURE DIRECTION 61
7.1 Summary 61
7.2 Future Direction 63
LIST OF REFERENCES 64
VITA 70

LIST OF TABLES

Table Page

Table 1.1: Comparison of s-drive with various existing actuators. 7

Table 2.1: Limits of operation. 16

Table 3.1: Coordinates of the elements in Figure 3.5 (a). 22

Table 5.1: Material properties of PZT5A [55]. 37

Table 5.2: Experimental displacements along with displacements calculated using analytical model and FEA model. 48

Table 5.3: Displacement of s-drive while switching between $+V_0$ to $-V_0$. 50

Table 5.4: Material properties of PVDF [56]. 51

Table 6.1: Channel flow piezo pen versus conventional dip pen. 60

Table 6.2: S-drive probe versus conventional probe. 60

LIST OF FIGURES

Figure Page

Figure 1.1: Two types of configurations for a nested array of building block. (a) shear-mode array, (b) axial-mode array. 1

Figure 1.2: Summary of $y_{\text{reported}}/L_{\max}$ of piezoelectric actuators from literature along with corresponding values for s-drive and its nested arrays calculated using the analytical model from this work. 6

Figure 1.3: Comparison of $y_{\text{reported}}/L_{\max}$ of s-drive and its nested axial-mode array with various actuation mechanisms from literature. 8

Figure 2.1: Simulated direct piezoelectric phenomenon. The left end of the beam corresponds to an anchor. The geometric properties are L = 25µm, $w = h$ = 2 µm. The application of a stress to either elongate or compress the beam by 0.1 µm induces a potential of $V = \pm 7$ V. 11

Figure 2.2: Simulated converse piezoelectric phenomenon. The left end of the beam corresponds to an anchor. The geometric properties are L = 25µm, $w = h$ = 2 µm and $V = \pm 40$ V. The expansion/contraction of 0.1 µm depending on the voltage polarity is shown above. 11

Figure Page

Figure 2.3: Basic converse piezoelectric phenomenon. (a) An application of electric field in the direction opposite to the dipole moment causes the material to contract along the poling axis and expand along the axes perpendicular to the poling axis. (b) The piezoelectric material expands in the poling axis direction axis and contracts along the axes perpendicular to the poling axis, when an electric field is applied in the direction of dipole moment.. 13

Figure 2.4: Bond diagram of a piezoelectric crystal PZT. The lower-left atom is the reference point of each diagram. The dashed circles represent the initial positions, and the solid spheres are possible deformed positions upon application of a vertical electric field (image based on concept presented in [51]). 14

Figure 2.5: Bond diagram of polyvinylidene fluoride (PVDF). The lower-left atom is the reference point of each diagram. The dashed circles represent the initial positions, and the solid spheres are possible deformed positions upon application of a vertical electric field (image based on concept presented in [54]). 15

Figure 3.1: In this 3D representation of the s-drive, the green colored region represents the piezoelectric material, blue colored region denotes the electrodes and '×' is the anchor point. In this design electrodes are configured such that an application of a voltage causes compression of two beams and extension of the other two beams [18]. This produces the so called s-drive as shown in Figure 3.2.................. 19

Figure 3.2: Simulation of s-drive using FEA solver COMSOL. The '×' corresponds to an anchor. The geometric properties are L = 300μm, w = h = 2 μm and V = 40 V. The bidirectional deflection of 42 μm depending on voltage polarity is shown above. ...20

Figure Page

Figure 3.3: Schematic cross section of s-drive. Here piezoelectric material is sandwiched between two metal layers. 21

Figure 3.4: A beam under pure bending. ρ is the radius of curvature, ds is the increment of beam length and $d\theta$ is the incremental subtended angle. 21

Figure 3.5: (a) shows the location of neutral axis, s-drives origin and centroid of s-drive, (b) shows the cross-section of s-drive considered and (c) shows the coordinates of elements 1 and 4. 23

Figure 3.6: Analytical model versus FEA model. For a s-drive of L = 300 μm, $h = w$ = 2 μm, h_m = 10 nm, E^p =127 GPa, E^m = 200 GPa, and $d_{31} = -274\times10^{-12}$ m/V the average relative error between analytical model and finite element analysis model is 5.5%. 26

Figure 3.7: Analytical model results. The effect of various dimensions on the s-drives displacement is shown above. The lateral displacement increases with increase in length and decreases with increase in width or thickness. 27

Figure 3.8: Effect of scaling of s-drive. 28

Figure 3.9: In this circuit the blue colored region represents the piezoelectric material, brown colored regions represent the electrodes and '×' is the anchor point. (b) shows the simulated s-drive with intermediate connectors, these connectors help in achieving higher displacement (c) shows the simulated s-drive without intermediate connectors and (d) shows the simulated s-drive with voltage applied only across the dark brown electrode. 29

Figure Page

Figure 4.1: Top view schematic of 1D array of s-drive. Here four s-drives are nested horizontally and if right most end is anchored as shown in (a) application of voltage causes a transverse deflection, and if bottom end is anchored as shown in (b) application of voltage causes a shear. The '×' indicates an anchor point, upon application of voltage across yellow electrode cause expansion and across red electrode cause compression. 31

Figure 4.2: Finite element analysis simulation of a 1D array of s-drives in an axial mode. (a) shows the 3D view of nesting 10 s-drives horizontally (b) shows the top view of the placement of 10 s-drives, the bottom right is fixed and on application of 20 V it deflects by 255 µm as shown in (c), and as shown in (d) for 40 V it deflects by 510 µm. 32

Figure 4.3: Finite element analysis simulation of a 1D array of s-drive operating in shear-mode. (a) shows the 3D view of the nesting 20 s-drives horizontally. The bottom of the actuator is an anchor and upon application of 40 V (b) 2 s-drives have a value of stiffness as 2.02 N/m deflect by 51 µm, (c) 10 s-drives have a value of stiffness as 10.1 N/m deflect by 51 µm, and (d) 20 s-drives have a value of stiffness as 20.2 N/m deflect by 51 µm. 33

Figure Page

Figure 4.4: Finite element analysis simulation of a 2D array of s-drive operating in axial-mode. It is possible to nest s-drive to form a 2D array, in this array the rightmost end is anchored. Here there are 20 s-drives in y direction and 4 s-drives in x direction. Upon application of 40 V it deflects by 1020 μm which is twenty times the deflection of a s-drive. Hence in axial-mode the increase in deflection is proportional to the number s-drives in y direction. 34

Figure 4.5: Finite element analysis simulation of a 2D array of s-drive operating in shear-mode. It is possible to nest s-drives to form a 2D array, in this array the bottom end is anchored. Here there are 40 s-drives in y direction and 2 s-drives in x direction. Upon application of 40 V it shears by 102 μm which is two times the shear of 1D array. Hence the increase in shear is proportional to the number s-drives in x direction. 35

Figure 5.1: Schematic of s-drive and nested s-drive in shear-mode and axial-mode. The blue regions represent the piezoelectric material and the brown regions in the top represent the electrodes with a voltage $V=V_0$ and the brown regions in the bottom represent the electrodes at $V = 0$. (a) shows the circuit of s-drive, (b) is the circuit of nested s-drive in shear-mode and (c) is the circuit of nested s-drive in axial-mode. The '×' indicates the anchor point. All the dimensions are in mm and the thickness of the structure is $h = 0.127$ mm..36

Figure Page

Figure 5.2: Top view of simulated s-drive and the 1D array of s-drive. The '×' indicates the anchor point and upon application of 50 V. (a) The s-drive deflects by 17.6 µm. (b) An array of three s-drives in shear mode shear by 17.6 µm. (c) Three s-drives nested in axial-mode magnify the defection by a factor of three. The material parameters of simulation are given in Table 5.1, and geometric properties are given in Figure 5.1. 38

Figure 5.3: Schematic cross section of s-drive. Here piezoelectric material is sandwiched between two metal layers. The gap between the sandwiches is air. y_{na},z_{na} correspond to the location of neutral axis from the s-drives origin. The coordinates of the nth element with reference to the s-drives origin are y_n , z_n. 39

Figure 5.4: Effect of applied voltage, various dimensions and nestability on s-drive's displacement (a) shows the change of displacement with applied voltage, (b) shows the change of displacement with thickness, gap, and width, (c) shows change of $y_{30}/L_{\max}$ with $L_{\max}$ and (d) change of $y_{30}/L_{\max}$ for the nested s-drive arrays. 42

Figure 5.5: Fabricated piezoelectric actuators. Laser-machined nested s-drives in an axial-mode (top), nested s-drives in a shear-mode (center) and s-drive (bottom) with electrode disconnects, electrical connections and reference point for measurements.......44

Figure 5.6: Experimental set up. The setup with two probes, voltage source for actuation and microscope with PC for measurements. 45

Figure 5.7: S-drive tip upon actuation. The position of the tip of s-drive before and after actuation. Upon application of 50 V, the s-drive deflects by 17.01 µm. 46

Figure Page

Figure 5.8: Lateral displacement versus applied voltage. The simulated results of s-drive and 1D arrays of s-drive compare well with the experimental measurements and analytical results with an average relative error of 6.3% in the range of 0-50 V. 47

Figure 5.9: S-drive tip upon actuation. The position of the tip of s-drive before and after actuation between +10 V and -10 V. The s-drive deflects by ±3.29 µm. 50

Figure 5.10: Fabrication steps: (a) shows the cutting of central holes, (b) shows the removal of electrode layers, and (c) shows the cutting of through holes to make the s-drive. 51

Figure 6.1: The basic design of nested s-drives to function as a new type of DPN or a probe. In this design, two pairs of arrays of s-drives in shear-mode are placed orthogonal to achieve the in-plane *x*, *y* movements and the piezostack achieves the out-of-plane movement in *z* direction. 55

Figure 6.2: Wiring for independent control of nested shear-mode arrays of s-drives. 56

Figure 6.3: In-plane movement of pen/probe. The figure shows the movement in the forward left direction, right direction, backward right direction, left direction 57

Figure 6.4: Out-of-plane movement of pen/probe. (a) shows the downward movement and (b) shows the upward movement. 58

SYMBOLS

$y_{reported}$	maximum reported actuator displacement
$L_{\max}$	maximum feature size
L	actuator length
W	actuator width
H	actuator thickness
P_{in}	average power per cycle
k	actuator stiffness
V	voltage
$v(x)$	transverse deflection
$u(x)$	axial deflection
$H_i(x)$	Hermitian shape function
S	strain energy
E_1	Young's modulus in axial direction
A	cross sectional area
I	moment of area
$\{F\}$	applied force
$\{q\}$	nodal displacement
$[k]_s$	individual stiffness matrix
$[m]_s$	individual mass matrix
$[c]_s$	individual damping matrix
$\overline{c}$	viscous damping per unit length

μ	viscosity of the fluid environment
Δ	distance between device and substrate
$[T]$	transformation matrix
θ	orientation of structure
$[K]$	system stiffness matrix
$[M]$	system mass matrix
$[C]$	system damping matrix
d_{31}	31 piezoelectric strain coefficient
(y_{na}, z_{na})	location of neutral axis
(y, z)	s-drives origin
(y_n , z_n)	coordinates of the nth element
h_m	thickness of metal layer
Δy_n	element width
Δz_n	element thickness
M_z	bending moment about the z-axis
$(EI)_{eff,z}$	effective flexural rigidity
k_c	cantilever stiffness
T_1^i	stress profile within the element
S_1^i	axial strain in the element

ABSTRACT

Chigullapalli, Aarti. Ph.D, Purdue University, December 2014. Modeling and Validation of S-drive: a Nestable Piezoelectric Actuator. Major Professors: Jason V. Clark, School of Electrical and Computer Engineering and Dimitrios Peroulis, School of Electrical and Computer Engineering.

This dissertation introduces a novel, nestable piezoelectric actuator, called the s-drive. In the s-drive actuator, the piezoelectric material is sandwiched between two conductors, and the electrodes are configured such that an application of a voltage causes an extension on two beams and compression on the other two beams to produce a large lateral deflection in the form of an 's' shape. The s-drive gets its name from the characteristic 's' shape that appears upon actuation. The designs of one-dimensional (1D) and two-dimensional (2D) arrays of axial-mode and shear-mode s-drives, for magnifying displacement and shear, are also presented in this work. Experimental results from the fabricated s-drive and its 1D nested arrays are presented for validation of the finite element analysis simulations and the developed analytical model of the s-drive and its nested arrays.

Additionally, the design of a new type of channel flow piezo pen, designed as a variation of s-drive, that is able to produce large deflections, with multiple degrees of freedom, and might handle multiple inks with the capability of writing on any surface in either wet or dry, clean or dirty environments is presented.

The s-drive, unlike electrostatic actuators, can work in relatively unclean environments, require lower power than electrothermal actuators, require lower driving voltages than electroactive polymers, and are geometrically configured to magnify small piezoelectric strains into larger deflections. These microactuators are expected to have applications in scanning probe microscopy, microassembly, nanolithography, and micro- and macro-scale robotics.

CHAPTER 1. INTRODUCTION

1.1 Nestability

In this dissertation, nestability is defined as the ability of an actuator to be used as a basic building block of a connected array of such actuators, which operate in unison to magnify deflection or force. Figure 1.1 shows the two configurations for a nested array of building blocks. In Figure 1.1, each black or white square in the checkerboard pattern represents one building block.

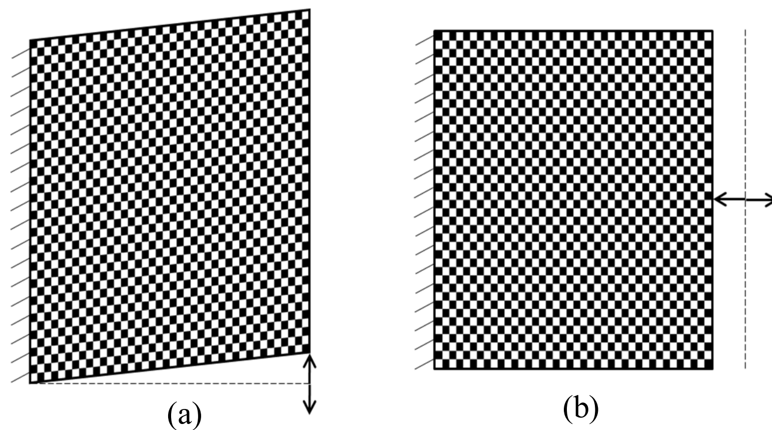

Figure 1.1: Two types of configurations for a nested array of building block. (a) shear-mode array, (b) axial-mode array.

Through nestability, it might be possible to bridge the gap between micro- and macro-scale sensors or actuators. These nested actuators or sensors might find applications in robotics, scanning probe microscopy, microassembly, nanolithography, variable diffraction gratings and bioengineering.

1.2 Motivation

Micro-electro-mechanical-systems (MEMS) capable of deflecting on the order of tens of microns and having nestability could find applications in robotics [1], optics [2], biomedical engineering [3], scanning probe microscopy, micro/nano-scale assembly and lithography [4]. The commonly used actuations mechanisms are: electrothermal [5-7], electrostatic [8], electroactive polymers [9], and piezoelectric [10].

Electrothermal actuators are actuated by an applied voltage that causes a current flow, which consequently leads to Joule heating, and thermal expansion. These actuators have been able to produce displacements on the order of tens of micrometers [5,11], but at the cost of high power consumption (up to tens of milliwatts) [6].

Electrostatic comb drives are actuated by generating an electrostatic surface pressure on the tips of conducting comb fingers by an applied voltage difference between the pair of opposing arrays of interdigitated comb fingers. Electrostatic comb drives have very low power consumption. However, they generate forces which rarely exceed 10 μN [6] in surface micromachined devices, and are often lower than 1 μN [12]. Hence, the displacements in these electrostatic actuators rarely go over 100 μm in resonant operation and 10 μm in nonresonant operation [6]. Even though larger displacements can be

achieved with a rather large actuator footprint, this is often not feasible due to space limitations [11]. Furthermore, since a single dust particle can immobilize an electrostatic actuator, a clean environment becomes quiet critical for reliable operation. Therefore, it is rather challenging for an electrostatic actuator to mechanically interact with environment outside the package.

Electroactive polymers are actuated by generating an electrostatic surface pressure on the polymer film by an applied voltage across the polymer thickness. This causes the polymer to compress along the thickness and expand along the cross-sectional area. They can generate large strains, over 50% [13], but their major drawback is the requirement of extremely-high activation fields above 100 MV/m [14]. Since electric shielding at such high fields is difficult, they cannot be used in wet and humid environments [15]. Such high fields may be associated with reliability issues.

In converse piezoelectric mechanism, an application of voltage to a piezoelectric material generates a strain Actuators working on these principles have advantages such as high energy density (~MJ/m^3), moderate driving fields, repeatability, and ability to work in any environment [16, 17]. However, the small electric field induced strains (0.1%-0.2%) of piezoelectric materials have limited their applications [15]. For example, achieving a 10 µm displacement requires an actuator size of 1 cm.

Since the piezoelectric materials have excellent properties, it is important to exploit these properties and build actuators that are nestable and capable of providing large deflections.

This dissertation presents a new type of nestable piezoelectric microactuator called the s-drive that is geometrically configured to magnify small piezoelectric strains into large deflections. The s-drive concept was introduced in [18]. In the s-drive actuator, the piezoelectric material is sandwiched between two conductors, and the electrodes are configured such that an application of voltage causes an extension on two beams and compression on the other two beams to produce a large lateral deflection in the form of an ‘s’ shape [18]. The s-drive gets its name from the characteristic ‘s’ shape that appears upon actuation

1.3 State of Art

In order to achieve large displacements with piezoelectric actuators, both internal and external amplification principles have been reported [19]. Internal systems include bimorph/multimorph piezoelectric actuator [20-30] and RAINBOW actuators [31]. Though these actuators have the ability to provide very high displacement (order of tens of microns), they have limited force. The most commonly used external amplification mechanisms are the hydraulic, mechanical amplifiers, and Moonie-type [32]. In the hydraulic mechanism the deformation of a piezoelectric disk causes the movement of a piston due to the volume change in fluid chamber [32-35]. The hydraulic actuators provide a peak amplification of 50:1, but they are relatively bulky [19] and due to fluid losses have a reduced response time [19]. For mechanical amplification, the input displacement is amplified by use of levers, bridges and various other transmission mechanisms [32, 36-42]. But, these are subject to wear from friction, which limits their lifetime and reliability in large environments. The Moonie actuator [43] has a

piezoelectric stack placed between two crescent shaped metal caps [19], such that the metal plates convert the stack's contraction into axial motion normal to the plate. This type of actuator exhibits a high force and high amplitude, but are complex to fabricate [19].

Figure 1.2 shows a comparison of reported piezoelectric actuators, based on the metric $y_{\text{reported}}/L_{\max}$, where y_{reported} is the reported actuator displacement and $L_{\max}$ is the maximum feature size. It can be seen that, to the best of authors' knowledge, the maximum $y_{\text{reported}}/L_{\max}$ from literature is approximately 0.02. This number depends on the properties of materials such as strain limit, dielectric breakdown and piezoelectric coefficients being used. The figure also shows the $y_{\text{reported}}/L_{\max}$ ratio for the s-drive and its 1D array nested in an axial-mode at an applied voltage of 30 V calculated from the analytical model. A 230 µm long s-drive, with PZT5A, upon application of 30 V deflects by 8.44 µm, which gives a ratio of 0.04. Nesting three s-drives in an axial-mode increases the deflection by a factor of three and hence the ratio for this is 0.12. It can be seen that with s-drive and its nested array high values of the $y_{\text{reported}}/L_{\max}$ metric can be achieved.

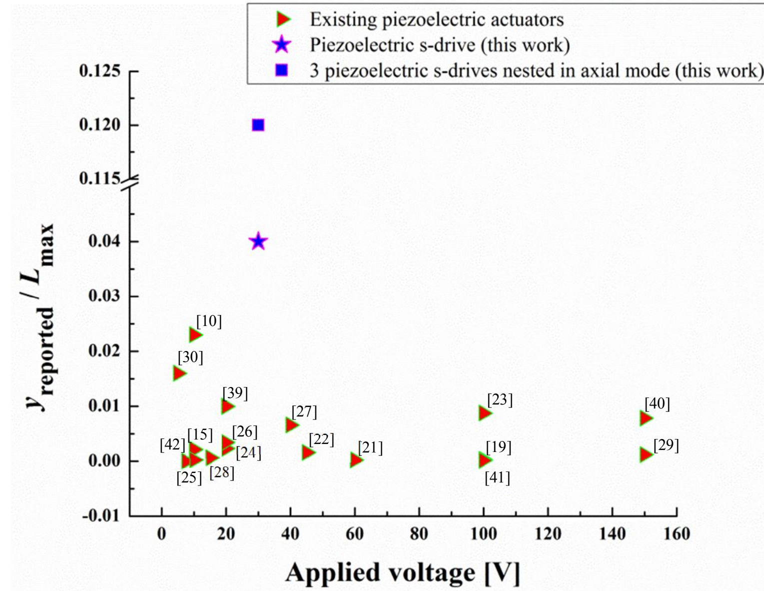

Figure 1.2: Summary of $y_{\text{reported}}/L_{\max}$ of piezoelectric actuators from literature along with corresponding values for s-drive and its nested arrays calculated using the analytical model from this work.

1.4 Other 'S' Shaped Actuators

Gilgunn et al. in [5] reported a lateral electrothermal actuator, which upon actuation formed an 's' shape. Their lateral electrothermal actuator is a multimorph structure with dielectric and metal interconnects [5]. The actuation of this actuator was due to the different coefficient of thermal expansion of aluminum metal interconnect and the silicon dioxide dielectric. Sato et al. in [44] reported a gas valve that was electrostatically actuated with a film that was in a 's' shape. In their actuator the ends of the s-shape film was attached to the top and bottom electrodes. The s-shaped film travelled due to the application of a voltage between the film and one end of the electrode.

1.5 Various Actuation Mechanisms

Table 1.1 shows the comparison of s-drive and various actuators taken from literature. Here L, w, h are the dimensions of the rectangular cell of the actuator. The average power per cycle P_{in} in Table 1.1, for electrothermal actuator was computed from the operating voltages and currents, for the other actuators it was computed by dividing the energy for charging and discharging the actuator by the time period of cycle.

Table 1.1: Comparison of s-drive with various existing actuators.

	Electrothermal s-drive	Electrothermal u-shaped	Electrothermal v-shaped	Electrostatic comb drive	Electroactive polymers	Piezo unimorph	Piezo s-drive
Author	Gilgunn [5]	Huang [7]	Que [5, 6]	Legtenberg [8]	Potter [9]	Kommepalli [10]	This work
Material	SiO_2-Al	Doped PolySi	Doped Si	Doped PolySi	Silicone	PZT	PZT 5A
L (µm)	400	200	410	1000	255×10^3	500	230
w (µm)	6.4	18.5	10.2	500	255×10^3	25	6
h (µm)	4.7	2	3	1.5	54×10^3	1.4	2
V (V)	4	5.5	12	20	3500	10	80
y_{reported} (µm)	2.5	14	10	40	1600	7	8.44
P_{in} (mW)	2	35	79	0.37	22.3	1.89	0.35
Metric	6×10^{-3}	0.07	0.02	0.04	6×10^{-3}	0.02	0.04

Figure 1.3, shows the comparison of s-drive with other reported actuation mechanisms based on the same metric $y_{\text{reported}}/L_{\max}$. Again, we note that this metric would depend on the material properties, driving voltage, actuator footprint, and specific requirements such as number of comb fingers for an electrostatic comb drive. It can be seen that the deflection ratio of piezoelectric s-drive is about half the value associated with an electrothermal u-shaped actuator, but the power consumed by the electrothermal u-shaped actuator is two orders of magnitude higher than that consumed by the s-drive. The $y_{\text{reported}}/L_{\max}$ of the s-drive is the same as electrostatic comb drive, but the

electrostatic comb drive has a larger actuator foot print. For the s-drive $y_{reported}/L_{max}$ can be increased by more than one order of magnitude through its capability of forming nested arrays.

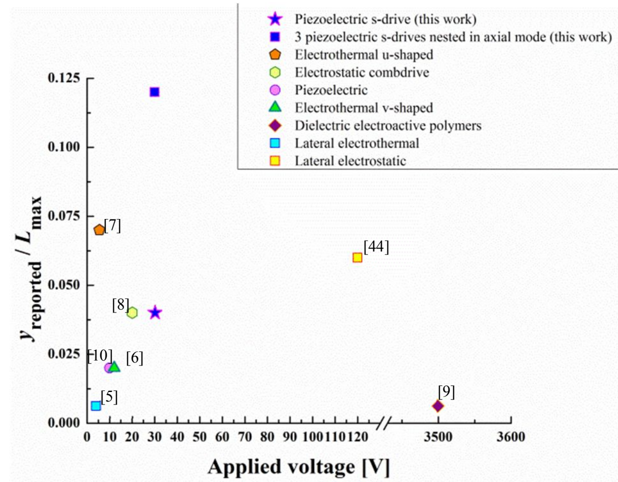

Figure 1.3: Comparison of $y_{reported}/L_{max}$ of s-drive and its nested axial-mode array with various actuation mechanisms from literature.

1.6 Previous Efforts of Nestability

V-shaped electrothermal actuator can be nested to magnify displacement or force. In [45], an array of paired v-shaped actuators was used to work as a variable diffraction grating. Each v-shape pair forms a rhombus as the nestable building-block. The array of ten u-shaped electrothermal actuators, for proportional magnification of force is presented in [46] and the possibility of building u-shaped electrothermal actuator into rotary or stepper motor, for displacement magnification is also presented [46]. However, these configurations have a large power consumption.

It is possible to stack electroactive polymers to magnify the strain. The stacking of four hundred layers of electroactive polymers is presented in [47]. This configuration

provided 50% compressive strain at 4.5 kV. The drawback of this configuration is the requirement of high driving fields.

The strain amplification of piezoelectric actuator with parallel guiding linkage amplifying structure is shown in [15]. The possibility of nesting three piezoelectric actuators with the mechanical amplification mechanism is also presented in [15]. But, the maximum reported displacement for this structure is 1.2 μm at 10 V.

1.7 Organization of Dissertation

The remainder of the dissertation is organized as follows: Chapter 2 describes the piezoelectric mechanism, and presents a few piezoelectric materials, with their structures, modes of failure and applications. The structural design, of a new type of nestable piezoelectric actuator called the s-drive [18], is presented in Chapter 3 and its nestability is presented in Chapter 4. Chapter 5 presents the validation of the s-drive concept, and includes experimental results from a fabricated s-drive and its nested arrays. Chapter 6 presents the possible application of the s-drive through the design of a new type of dip pen nanolithography called the channel flow piezo pen that is able to produce large deflections, with multiple degrees of freedom, with the capability of writing on many surfaces. Chapter 7 summarizes the contributions from this work with the recommendations for future work.

CHAPTER 2. THEORY OF PIEZOELECTRICITY

In the piezoelectric effect energy is transferred between electric and mechanical domain and vice versa. In the direct piezoelectric effect, the piezoelectric materials generate electric potential upon application of strain. In the converse piezoelectric effect, the piezoelectric materials generate a strain upon application of electric field. This chapter gives a brief description of the piezoelectric mechanism, and introduces few piezoelectric materials, with their structures, modes of failure and applications.

2.1 Piezoelectric Mechanism

In this section, a brief description of the basic piezoelectric mechanism is given. The word 'piezo' in Greek means pressure, therefore the meaning of the word piezoelectricity is 'pressure electricity' [48]. Piezoelectricity is the interaction between mechanical and electrical systems in asymmetric crystals. Application of mechanical stress on certain materials induces an electric charge as shown in Figure 2.1, and this phenomenon known as the direct piezoelectric effect is generally employed in sensor applications. Actuator applications use the converse piezoelectric effect shown in Figure 2.2, where a piezoelectric material becomes strained upon application of an external electric field [49].

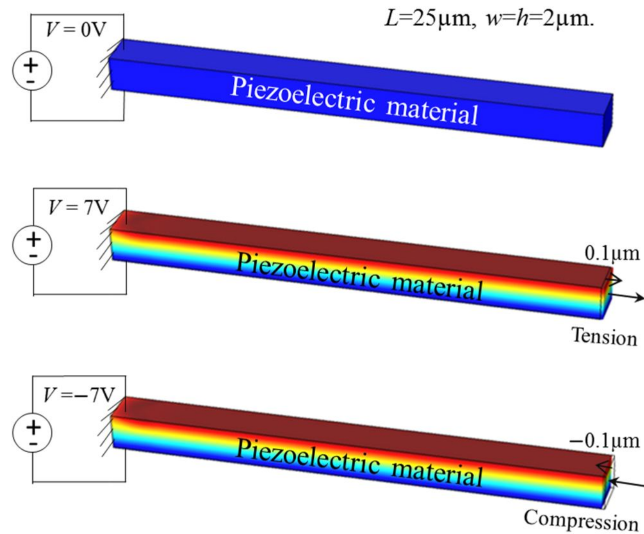

Figure 2.1: Simulated direct piezoelectric phenomenon. The left end of the beam corresponds to an anchor. The geometric properties are L = 25μm, w = h = 2 μm. The application of a stress to either elongate or compress the beam by 0.1 μm induces a potential of V = ±7 V.

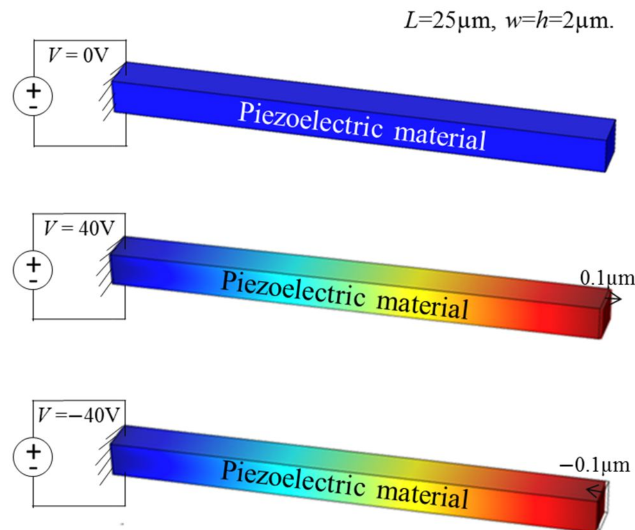

Figure 2.2: Simulated converse piezoelectric phenomenon. The left end of the beam corresponds to an anchor. The geometric properties are L = 25μm, w = h = 2 μm and V = ±40 V. The expansion/contraction of 0.1 μm depending on the voltage polarity is shown above.

2.2 Piezoelectric Materials

Piezoelectric materials are materials that are able to generate a voltage due to an applied strain, and generate a strain due to an applied voltage. Some of the piezoelectric materials are piezoelectric ceramics such as lead zirconate titanate crystals (PZT) and piezoelectric polymers, such as polyvinylidene fluoride (PVDF). Typically, piezoelectric materials comprise of various ions that are chemically bonded to each other such that the arrangement of ions leads to a resultant positive charge and negative charge on either sides, forming a dipole along the direction called the poling axis. When an external voltage applied across the poling axis sets up the electric field in the direction opposite to the material's dipole moment as shown in Figure 2.3(a), the electrical forces act towards the center of the dipole, which cause the material to contract along the poling axis. In order to maintain the equilibrium bond distances, the ionic forces within the material lead to an expansion in the axes perpendicular to the poling axis. Whereas, if the external voltage applied across the poling axis sets up an electric field in the direction of material's dipole moment as shown in Figure 2.3(b), the electrical forces act away from the center of the dipole that cause the expansion of the piezoelectric material in the poling axis direction and the ionic forces lead to a contraction along the axes perpendicular to the poling axis.

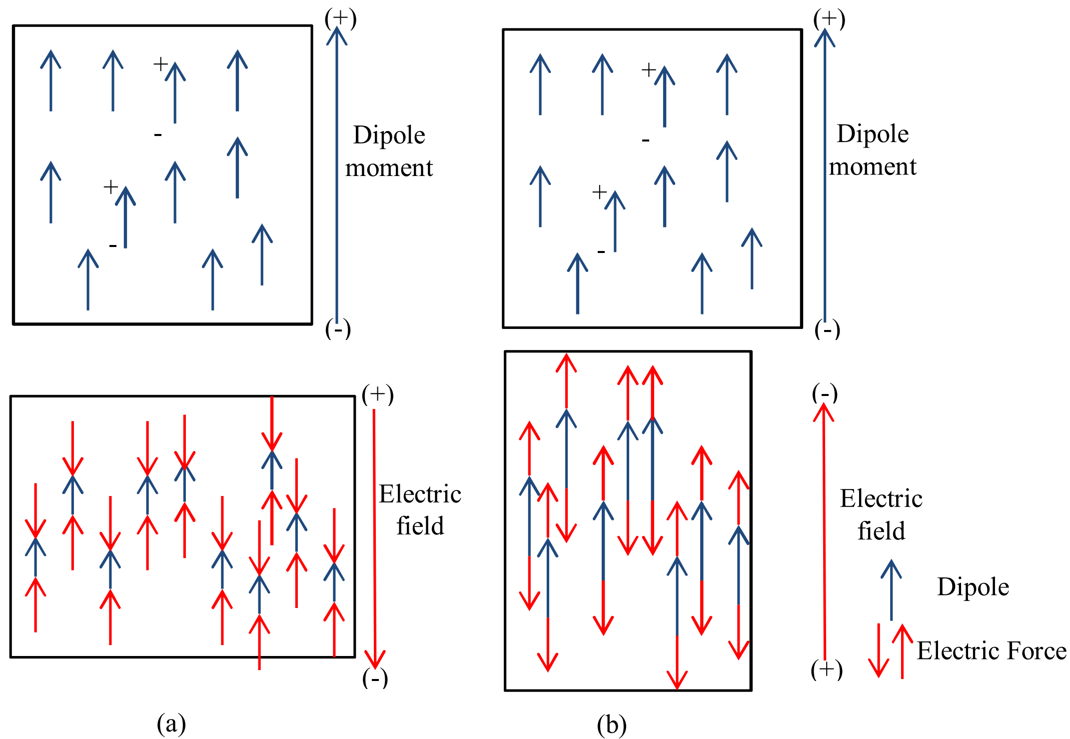

Figure 2.3: Basic converse piezoelectric phenomenon. (a) An application of electric field in the direction opposite to the dipole moment causes the material to contract along the poling axis and expand along the axes perpendicular to the poling axis. (b) The piezoelectric material expands in the poling axis direction and contracts along the axes perpendicular to the poling axis, when an electric field is applied in the direction of dipole moment.

2.2.1 Piezoelectric Ceramics (PZT)

A traditional piezoelectric ceramic PZT [50, 51] is a mass of perovskite ceramic crystal, with a chemical formula $Pb(Zr_xTi_{1-x})$ where depending on the fabrication process x lies between 0 and 1. PZT has a tetragonal structure where lead cations occupy the corners of the cuboid, oxygen anions form an octahedron within the cuboid and a titanium or zirconium ion is at an offset from the center of the oxygen octahedron as shown in Figure 2.4(a). In this arrangement of ions, the centroid of positive charges does not coincide with the centroid of negative charges, and thus forms a dipole. For the molecular structures shown in Figure 2.4(a), a

vertically applied electric field causes Zr_xTi_{1-x} to vertically displace, which affects bond angles and or lengths. The changes in bond angles cause the structure of the molecule to vertically compress and horizontally expand, illustrated by solid spheres in Figure 2.4(b). By reversing the polarity of the electric field, the molecular structure vertically elongates and horizontally compresses. By removing the field, the structure returns to its original state, illustrated by dashed circles in Figure 2.4(b).

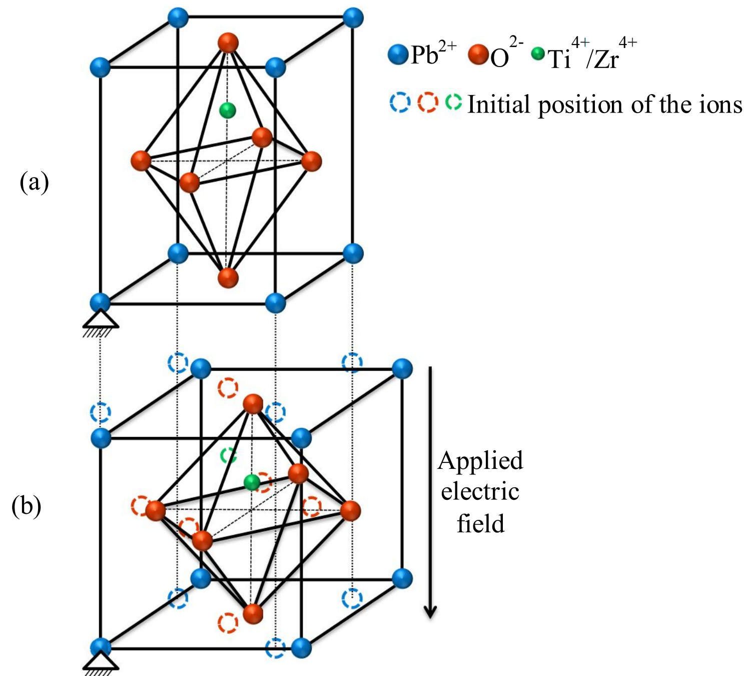

Figure 2.4: Bond diagram of a piezoelectric crystal PZT. The lower-left atom is the reference point of each diagram. The dashed circles represent the initial positions, and the solid spheres are possible deformed positions upon application of a vertical electric field (image based on concept presented in [51]).

2.2.2 Polyvinylidene Fluoride (PVDF)

Polyvinylidene fluoride (PVDF) [52-54] has the chemical formula $(CH_2\text{-}CF_2)_n$ as shown in Figure 2.5(a). This material is manufactured in the form of thin sheets that are stretched along the direction of maximum carbon atoms and poled along the thickness of the sheet. If the atoms are oriented as shown in Figure 2.5(a), dipole

moment is directed from net negative charge due to fluorine atoms to net positive charge due to hydrogen atoms. For the molecular structures shown in Figure 2.5(a), a vertically-applied electric field causes H/F to vertically displace, which affects bond angles and or lengths. The changes in bond angles cause the structure of the molecule to vertically compress and horizontally expand, illustrated by solid spheres in Figure 2.5(b). By reversing the polarity of the electric field, the molecular structure vertically elongates and horizontally compresses. By removing the field, the structure returns to its original state, illustrated by dashed circles in Figure 2.5 (b).

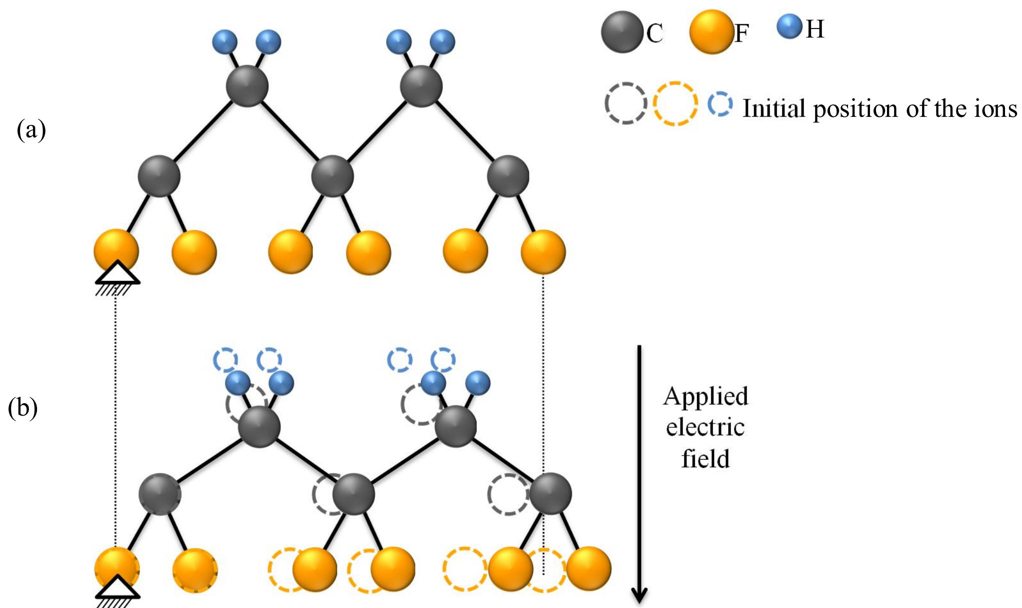

Figure 2.5: Bond diagram of polyvinylidene fluoride (PVDF). The lower-left atom is the reference point of each diagram. The dashed circles represent the initial positions, and the solid spheres are possible deformed positions upon application of a vertical electric field (image based on concept presented in [54]).

2.3 Limits of Operation

While designing piezoelectric actuators, the important limits that need to be considered are the piezoelectric materials strain limit, dielectric breakdown and Curie temperature. Table 2.1 gives these limits for PZT [55] and PVDF [56, 57].

Table 2.1: Limits of operation.

	PZT	**PVDF**
Strain limit	0.1%-0.2%	4%
Dielectric breakdown [V/µm]	40	80
Curie temperature [°C]	350	103
31 Piezoelectric strain coefficient d_{31} [m/V]	-274×10^{-12}	-21×10^{-12}

The strain limit of piezoelectric material ranges from 0.1%-0.2% [15] for many crystals to 4% [56] for piezo polymers. Such limits should be considered when designing the piezoelectric actuators.

The other limits to be considered are the dielectric breakdown limit and Curie temperature. Piezoelectric materials when operated above these limits, lose their asymmetric structures and hence the piezoelectric effect. The actuators made from PZT should be driven with electric fields below 40 V/µm and must operate at temperatures below 350 °C [58]. The actuators made from PVDF should be driven with electric fields below 80 V/µm and should not reach temperatures above 103 °C [59].

The piezoelectric strain coefficient of PZT is an order of magnitude higher than that of PVDF. Hence, for the same applied voltage PZT gives displacements an order of magnitude higher than that of PVDF.

The strain limit and dielectric breakdown of PVDF (4%, 80 V/µm) is higher than that of PZT (0.1-0.2%, 40 V/µm). But, its piezoelectric strain coefficient is an order of magnitude lower than that of piezo crystal and, hence, for the same applied voltage the displacement achieved by piezo polymer PVDF is an order of magnitude lower than that of the piezo crystal. The Curie temperature of PZT is three times the Curie temperature of PVDF. Hence, PZT works better for fabrication methods such as

laser machining that involve generation of high temperature. The material should be chosen based on the applications and selected fabrication method.

2.4 Applications of Piezoelectric Materials

Some common piezoelectric applications include positioners, energy harvesters, vibrators, motors, and valves. For example, large bulk 3D positioning platforms for atomic force microscope [4] use in-plane scanners for the *xy* plane movement and cantilever's position in *z*-axis is controlled by the stacked piezoelectric actuator. In energy harvesting [60], the mechanical energy is converted to electrical energy with piezoelectric material. The vibrating alarm feature of some of the mobile phone devices [61] uses a piezoelectric vibration actuator that convert's electrical energy into mechanical vibration. Some cameras of mobile phone devices [62], where high resolution images are obtained. The precise lens movements in either the forward or backward direction are produced by a piezoelectric actuator, based on the signal given by the position-sensory circuit. In a fuel injection system [63], a piezoelectric micro mass flow controller is used for feeding the liquid fuel which reduces the fuel consumption by more than 20% [64].

CHAPTER 3. S-DRIVE A NESTABLE PIEZOELECTRIC ACTUATOR

Large deflection actuators capable of forming nested actuators may find applications in robotics, scanning probe microscopy, lithography, micro-scale assembly and nano-scale assembly [18]. Due to the small strain limits of piezoelectric materials most of the existing piezoelectric actuators have relatively small deflections. This chapter presents a new type of piezoelectric actuator called the s-drive [18] that is nestable and is geometrically configured to magnify the small piezoelectric strains into large deflections. The s-drive gets its name from the characteristic ‘s’ shape that appears upon actuation. The s-drive has the ability to actuate and sense, can physically interact with the environment, can work with a single voltage source, can have a single anchor point, requires low power, can be fabricated from ceramic or polymer, can be flexible and can help in bridging the gap between micro and macro scale actuators through nestability. Compared to the arrays of some of the most commonly used actuation mechanisms, the array of s-drives can work in either axial mode or shear mode, and can expand or compress. This chapter covers the s-drive concept with simulation results and analytical modeling. The next chapter introduces the performance of nested s-drives.

3.1 S-Drive Concept

In this actuator, the piezoelectric material is sandwiched between two conductors, and the electrodes are configured such that an application of voltage cause an extension on two beams and compression on the other two beams to produce a large lateral deflection in the form of an 's' shape [18], as shown in Figure 3.2. The s-drive gets its name from this characteristic 's' shape that appears upon actuation.

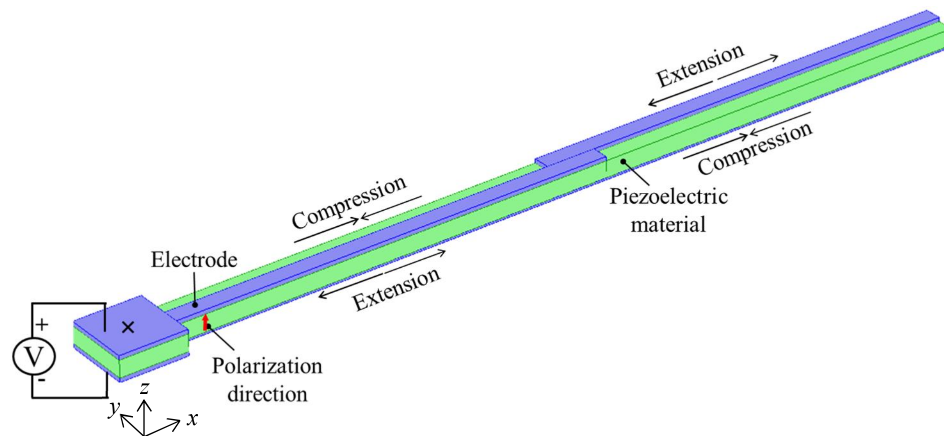

Figure 3.1: In this 3D representation of the s-drive, the green colored region represents the piezoelectric material, blue colored region denotes the electrodes and '×' is the anchor point. In this design electrodes are configured such that an application of a voltage causes compression of two beams and extension of the other two beams [18]. This produces the so called s-drive as shown in Figure 3.2.

3.2 Finite Element Analysis Modeling of S-drive

The 3D piezo module of COMSOL Multiphysics was used for the finite element analysis (FEA) simulations. The left boundary denoted by '×' is fixed, and depending on the voltage polarity, the top and bottom boundaries are either at ground or have an electric potential. The simulated s-drive is presented in Figure 3.2.

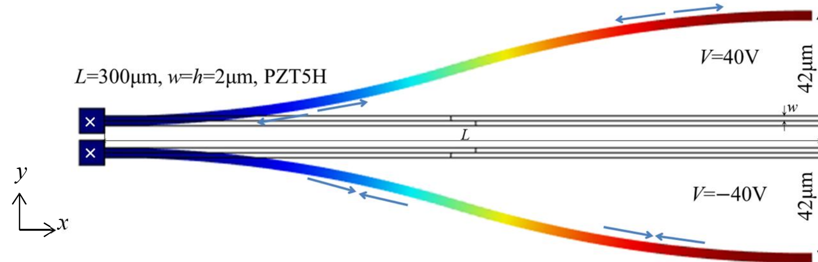

Figure 3.2: Simulation of s-drive using FEA solver COMSOL. The '×' corresponds to an anchor. The geometric properties are L = 300µm, w = h = 2 µm and V = 40 V. The bidirectional deflection of 42 µm depending on voltage polarity is shown above.

3.3 Analytical Modeling of S-drive

This section presents the analytical model for calculating the lateral displacement and stiffness of s-drive without a gap as shown in Figure 3.2. Gilgunn in [5] presented an analytical model for CMOS thermal multimorph. Since the s-drive has multilayers, as shown in Figure 3.3, a similar formulation can used for deriving the analytical stiffness and displacement.

3.3.1 Assumptions

S-drive as shown in Figure 3.3 has a piezoelectric material between thin metal electrodes. In this analysis the s-drive is divided into rectangular element as shown in Figure 3.3.

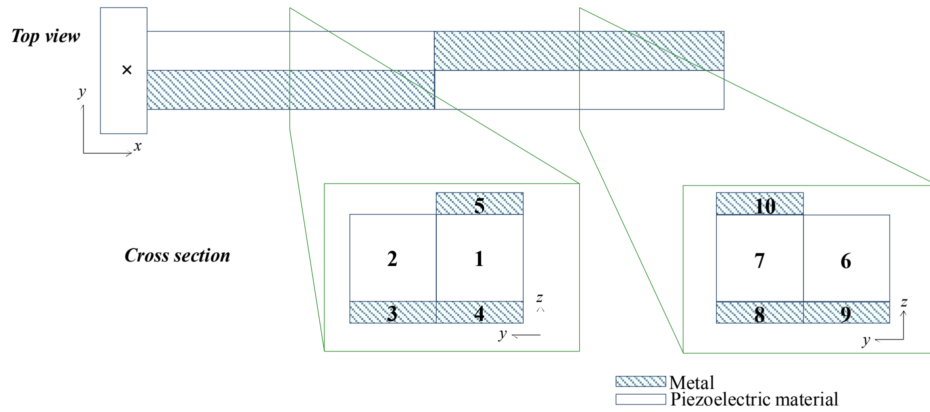

Figure 3.3: Schematic cross section of s-drive. Here piezoelectric material is sandwiched between two metal layers.

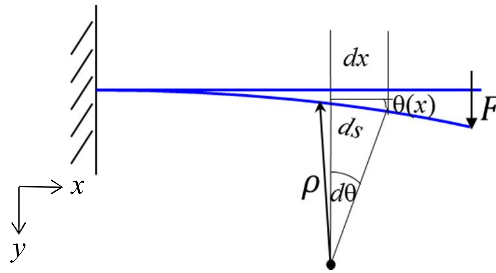

Figure 3.4: A beam under pure bending. ρ is the radius of curvature, ds is the increment of beam length and $d\theta$ is the incremental subtended angle.

For small angle approximation, the radius of curvature for beam shown in Figure 3.4 is given by

$$\frac{1}{\rho} = \frac{d^2 y}{dx^2} \ . \tag{3.1}$$

For large angle approximation, the radius of curvature for beam shown in Figure 3.4 is given by

$$\frac{1}{\rho} = \frac{d^2 y / dx^2}{\left[1 + \left(dy/dx\right)^2\right]^{3/2}} \ . \tag{3.2}$$

The analytical model of s-drive was developed using the small angle approximation.

3.3.2 Lateral Displacement and Stiffness

The curvature of s-drive due to a bending moment is given by

$$\frac{d^2y}{dx^2} = \frac{M_z}{(EI)_z} \ , \tag{3.3}$$

where M_z is the z-axis bending moment due to the axial stress, the flexural rigidity is $(EI)_z$, with E being the Young's modulus in the axial direction and I the second moment of area. Integration of (3.3) gives the lateral displacement of the s-drive as

$$y(x) = \frac{M_z x^2}{4(EI)_z} \ . \tag{3.4}$$

The stiffness of s-drive is calculated using

$$k = \frac{3(EI)_z}{L^3} \ . \tag{3.5}$$

The following sections provide the derivation of moment about z-axis and flexural rigidity.

Neutral axis: The neutral axis locates the radius of curvature of the actuator. If the bending moment is calculated about the neutral axis, the contribution of axial deformation can be neglected. In Figure 3.5(a) its placement is shown as y_{na}, z_{na}.

Table 3.1: Coordinates of the elements in Figure 3.5 (a).

Element#	y_n	z_n	Δy_n	Δz_n	E^n
1	0	h_m	w	h	E^p
2	w	h_m	w	h	E^p
3	w	0	w	h_m	E^m
4	0	0	w	h_m	E^m
5	0	$h+h_m$	w	h_m	E^m

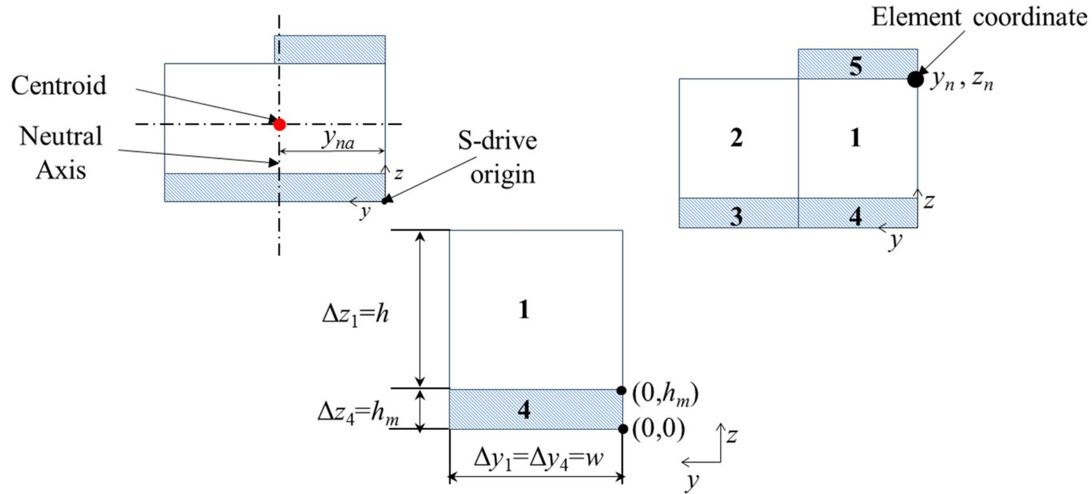

Figure 3.5: (a) shows the location of neutral axis, s-drives origin and centroid of s-drive, (b) shows the cross-section of s-drive considered and (c) shows the coordinates of elements 1 and 4.

The location of centroid from the s-drive's origin can be calculated by

$$y_{na}=\frac{\sum_{elements}\int_{z_n}^{z_n+\Delta z_n}\int_{y_n}^{y_n+\Delta y_n}E^n y\,dy\,dz}{\sum_{elements}\int_{z_n}^{z_n+\Delta z_n}\int_{y_n}^{y_n+\Delta y_n}E^n\,dy\,dz}, \tag{3.6}$$

$$y_{na}=\frac{\sum_{elements}E^n\left.\frac{y^2}{2}\right|_{y_n}^{y_n+\Delta y_n}\left.z\right|_{z_n}^{z_n+\Delta z_n}}{\sum_{elements}E^n\left.y\right|_{y_n}^{y_n+\Delta y_n}\left.z\right|_{z_n}^{z_n+\Delta z_n}}=\frac{\sum_{elements}E^n\Delta y_n\Delta z_n\left(2y_n+\Delta y_n\right)}{2\sum_{elements}E^n\Delta y_n\Delta z_n}, \tag{3.7}$$

where (y_n, z_n) are the nth element coordinates from the s-drives origin (y,z), and Δy_n, Δz_n are the element width and thickness respectively, and E^n is the nth element's Young's

modulus in the axial direction. A similar equation can be written for z_{na}. Substituting the coordinates of the elements from Table 3.1 in (3.7) gives

$$y_{na} = \frac{w\left(4E^{p}h + 5E^{m}h_{m}\right)}{2\left(2E^{p}h + 3E^{m}h_{m}\right)}. \tag{3.8}$$

Flexural rigidity: The flexural rigidity for multilayer structure about the z-axis can be calculated from

$$\left(EI\right)_{z} = \sum_{elements} \int_{z_n - z_{na}}^{z_n + \Delta z_n - z_{na}} \int_{y_n - y_{na}}^{y_n + \Delta y_n - y_{na}} E^{n} y^{2} dy dz\,, \tag{3.9}$$

Substituting the coordinates from Table 4.1 in (3.9) gives

$$\left(EI\right)_{z} = \frac{E^{p}wh}{3}\left(8w^{2} + 6y_{n}^{2} - 12wy_{n}\right) + \frac{E^{m}wh_{m}}{3}\left(9w^{2} + 9y_{n}^{2} - 15wy_{n}\right). \tag{3.10}$$

Bending Moment: For a multilayer structure the z-axis bending moment due to axial stress can be calculated from

$$M_{z} = \sum_{elements} \int_{z_n - z_{na}}^{z_n + \Delta z_n - z_{na}} \int_{y_n - y_{na}}^{y_n + \Delta y_n - y_{na}} T_{1}^{n} y dy dz = \sum_{elements} \frac{T_{1}^{n}\Delta z_{n}\Delta y_{n}\left(\Delta y_{n} + 2y_{n} - 2y_{na}\right)}{2}, \tag{3.11}$$

where, T_1^n is the stress profile within an element. The stress in the piezoelectric element for compression is $T_1^n = E^p S_1^n - d_{31}E^p \frac{V}{h}$ [65] and for extension is $T_1^n = E^p S_1^n + d_{31}E^p \frac{V}{h}$ [65], and stress in metal layers is $T_1^n = -E^m S_1^n$ for compression and $T_1^n = +E^m S_1^n$ for extension. E^p is the piezoelectric material's Young's modulus in the axial direction, S_1^n is the axial strain in the element, d_{31} is the peizoelectric coefficient for length change in

m/V, voltage applied across the piezoelectric material thickness is V, h is the piezoelectric material's thickness, and E^m is the Young's modulus of the metal layer. $S_1^n = 0$ as the bending moment is calculated with the neutral axis as the reference. By substituting the coordinates from Table 3.1, and the stress terms in (3.11) we get

$$M_z = \frac{whd_{31}E^pV\left(w-2y_{na}\right)}{2h}. \tag{3.12}$$

Substituting (3.10) and (3.12) in (3.4) gives

$$y\left(L\right) = \frac{3whd_{31}E^pV\left(w-2y_{na}\right)L^2}{8h\left\{E^pwh\left(8w^2+6y_{na}^2-12wy_{na}\right)+E^mwh_m\left(9w^2+9y_{na}^2-15wy_{na}\right)\right\}}. \tag{3.13}$$

Substituting (4.10) in (4.5) gives

$$k = \frac{w\left\{E^ph\left(8w^2+6y_{na}^2-12wy_{na}\right)+E^mh_m\left(9w^2+9y_{na}^2-15wy_{na}\right)\right\}}{L^3}. \tag{3.14}$$

Substituting L = 300 μm, h = w= 2 μm, h_m = 10 nm, E^p = 127 GPa, E^m = 200 GPa, and $d_{31} = -274\times10^{-12}$ m/V, in (4.14) gives k = 0.15 N/m. FEA simulation gives k_{FEA} = 0.154N/m. The relative error between analytical stiffness and FEA stiffness is 2%.

From Figure 3.6 it can be seen that the analytical model predicts displacements close to the displacements of finite element analysis model within an average relative error of 6.3% (0-80V). The method of discretization is different in FEA model and analytical model. In analytical model the cross-section is divided into five elements, while in FEA the s-drive is discretized into fifteen thousand elements.

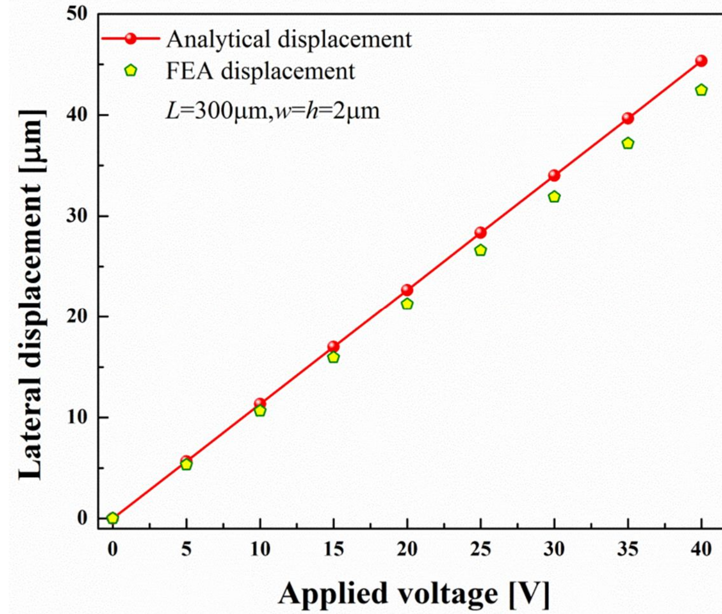

Figure 3.6: Analytical model versus FEA model. For a s-drive of L = 300 µm, $h = w = 2$ µm, h_m = 10 nm, E^p =127 GPa, E^m = 200 GPa, and $d_{31} = -274 \times 10^{-12}$ m/V the average relative error between analytical model and finite element analysis model is 5.5%.

From Figure 3.7 it can be seen that the s-drives lateral displacement can be increased by increasing the s-drives length, or decreasing the width or decreasing the thickness. But, while changing these dimensions, the fabrication method and material properties should be taken into consideration.

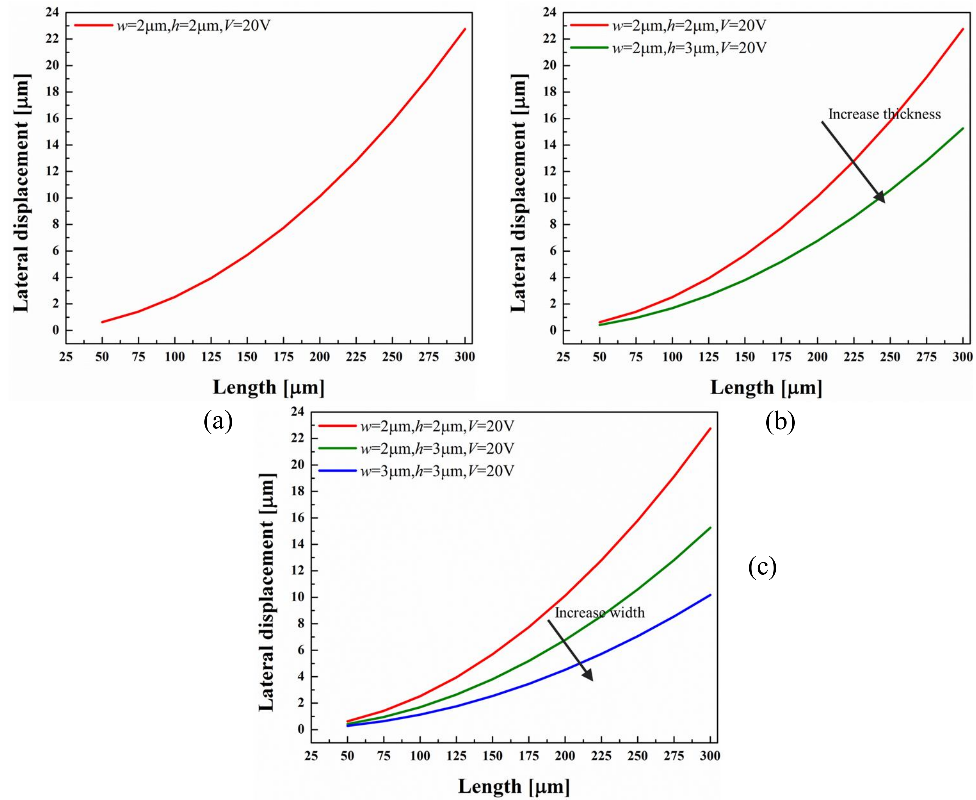

Figure 3.7: Analytical model results. The effect of various dimensions on the s-drives displacement is shown above. The lateral displacement increases with increase in length and decreases with increase in width or thickness.

3.4 Effect of Scaling

The s-drive shown in Figure 3.2 was scaled in 3D from 0.1 to 100. For the smallest scaling factor (SF) of 0.1, the voltage below dielectric breakdown is 8 V. Hence, for this analysis a constant voltage of 8 V was applied for all the SFs. From Figure 3.8 it can be seen that the ratio of lateral displacement to length of s-drive decreases as the scaling increases. Hence, it is better to have smaller s-drives.

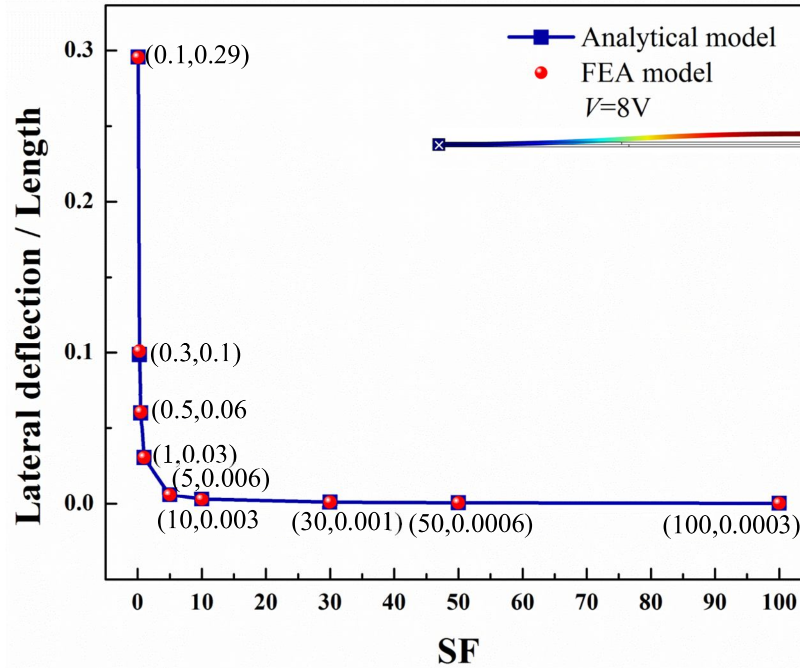

Figure 3.8: Effect of scaling of s-drive.

3.5 Other Possible Designs of S-drive

The three other possible designs of s-drive are shown in Figure 3.9, Figure 3.9(a) shows the circuit of the s-drive, the simulated s-drive with intermediate connectors is shown in Figure 3.9(b), these connectors help in achieving higher displacement, the simulated s-drive similar to Figure 3.9(b) without the two couplings is shown in Figure 3.9(c) and the simulated s-drive with voltage applied only across the dark brown electrode of Figure 3.9(a) is shown in Figure 3.9(d).

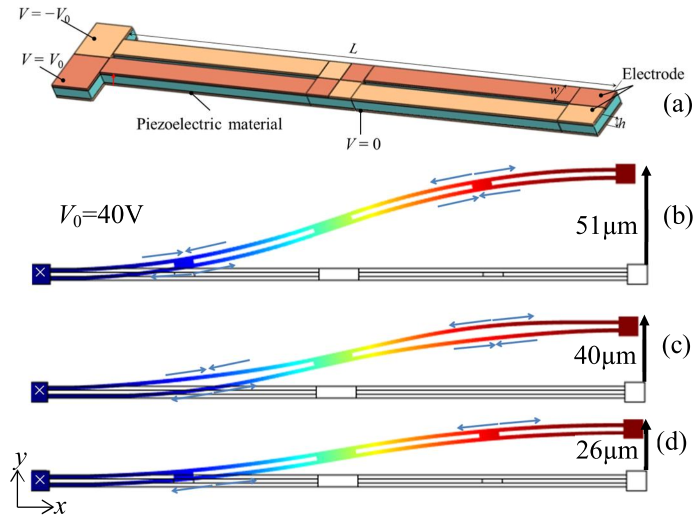

Figure 3.9: In this circuit the blue colored region represents the piezoelectric material, brown colored regions represent the electrodes and '×' is the anchor point. (b) shows the simulated s-drive with intermediate connectors, these connectors help in achieving higher displacement (c) shows the simulated s-drive without intermediate connectors and (d) shows the simulated s-drive with voltage applied only across the dark brown electrode.

CHAPTER 4. NESTABILITY

Previous chapter presented a new type of fixed guided piezoelectric microactuator s-drive [18]. This chapter presents the nestability of s-drive to achieve magnified in-plane deflections, both shear and translation, for the same applied voltage. In this work nestability is defined as the ability of an actuator to form the basic building block of a connected array of such actuators, which actuate in unison to magnify deflection. The following sections present the design, and simulation of 1D and 2D arrays of s-drive.

4.1 1D Array

Forming an array of an actuator helps in magnification of displacement or force and hence bridging the gap between micro and macro scale. A 1D or 2D array of s-drive has the ability to magnify the displacement and force and hence the s-drive is highly nestable. This section presents the simulation and analytical model for a 1D array of s-drive that work in either axial-mode or shear-mode.

Figure 4.1 shows the schematic of a 1D array of s-drives that can, work in axial-mode [18], as shown in Figure 4.1(a), or shear-mode, as shown in Figure 4.1(b). In Figure 4.1 the bottom electrode (not shown in the figure) is at $V = 0$, the top yellow electrode is at voltage $V = V_0$ and the top red electrode is at voltage $V = -V_0$.

If the rightmost end of the array is anchored as shown in Figure 4.1(a), the array will achieve magnified transverse deflection for the same applied voltage. If the bottom end of the array is anchored as shown in Figure 4.1(b), the array will shear upon application of voltage.

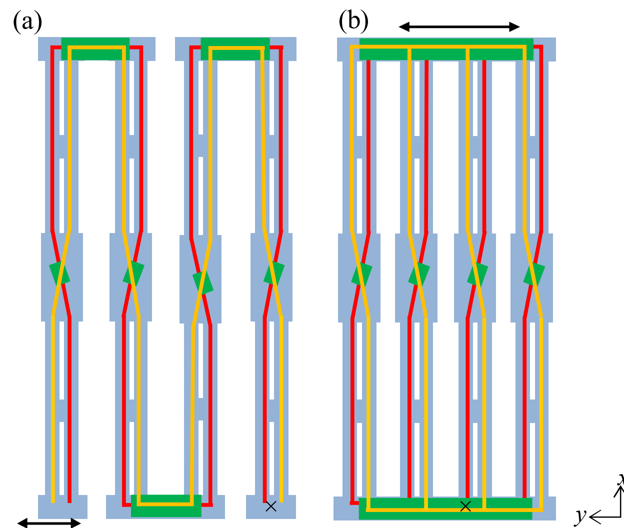

Figure 4.1: Top view schematic of 1D array of s-drive. Here four s-drives are nested horizontally and if right most end is anchored as shown in (a) application of voltage causes a transverse deflection, and if bottom end is anchored as shown in (b) application of voltage causes a shear. The '×' indicates an anchor point, upon application of voltage across yellow electrode cause expansion and across red electrode cause compression.

4.1.1 Axial-Mode

Figure 4.2 shows the finite element analysis simulation of a 1D array of 10 s-drives in an axial-mode [18] using COMSOL 4.3a. In this mode of operation, the magnification of displacement is proportional to the number of s-drives in the y direction.

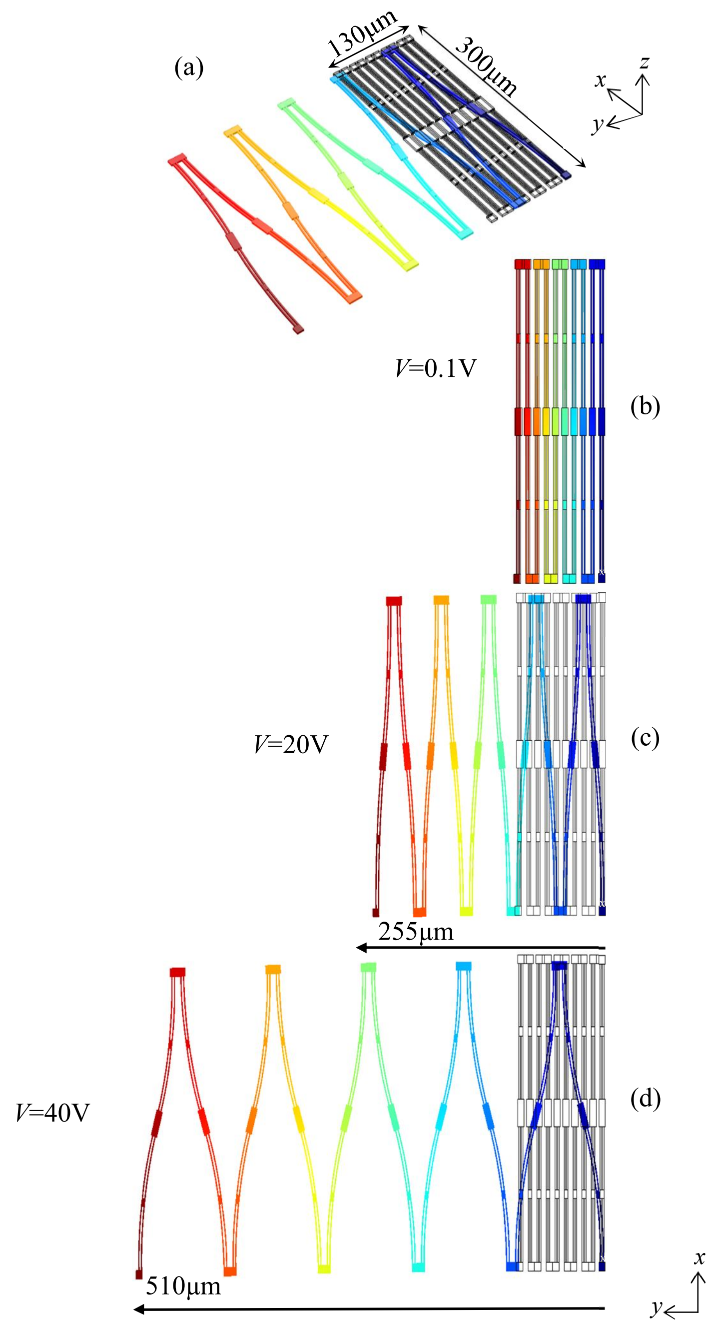

Figure 4.2: Finite element analysis simulation of a 1D array of s-drives in an axial mode. (a) shows the 3D view of nesting 10 s-drives horizontally (b) shows the top view of the placement of 10 s-drives, the bottom right is fixed and on application of 20 V it deflects by 255 μm as shown in (c), and as shown in (d) for 40 V it deflects by 510 μm.

The displacement of an array can be increased by either increasing the voltage or by increasing the number of s-drives [18]. Figure 4.2(c) and (d) show the first way of increasing displacement i.e. doubling of voltage for doubling of displacement.

4.1.2 Shear-Mode

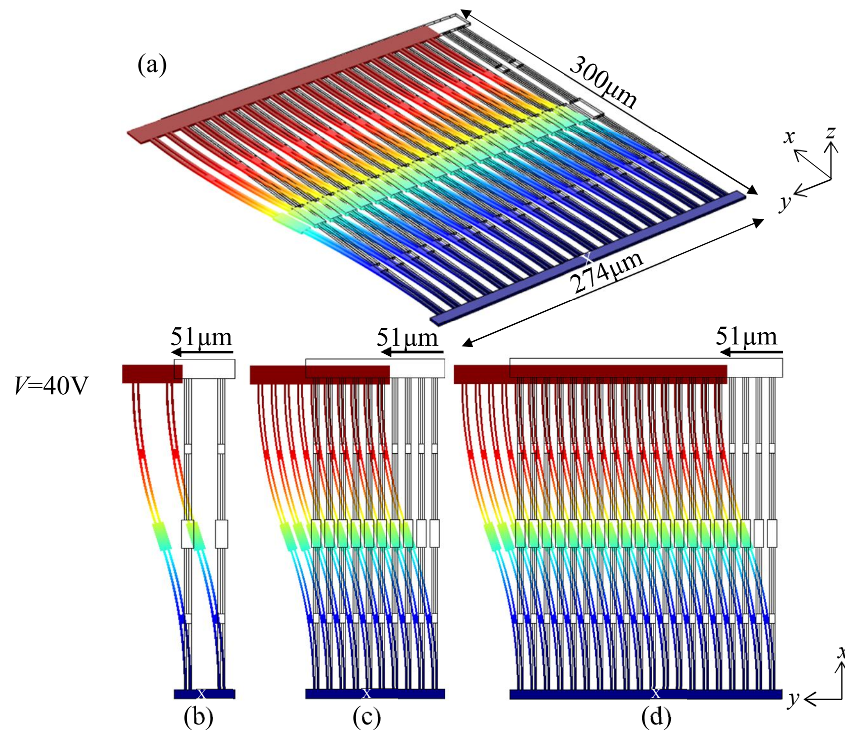

Figure 4.3: Finite element analysis simulation of a 1D array of s-drive operating in shear-mode. (a) shows the 3D view of the nesting 20 s-drives horizontally. The bottom of the actuator is an anchor and upon application of 40 V (b) 2 s-drives have a value of stiffness as 2.02 N/m deflect by 51 μm, (c) 10 s-drives have a value of stiffness as 10.1 N/m deflect by 51 μm, and (d) 20 s-drives have a value of stiffness as 20.2 N/m deflect by 51 μm.

Figure 4.3 shows the 1D array of s-drives operating in shear-mode. In this 1D array configuration same amount of displacement independent of number of s-drives can be achieved.

4.2 2D Array

It is also possible to nest the s-drive in both *x* and *y* directions, to form a 2D array, which works in unison, similar to muscle cells in animals. This section presents the simulation of 2D array of s-drive that can work in axial and shear-mode.

4.2.1 Axial-Mode

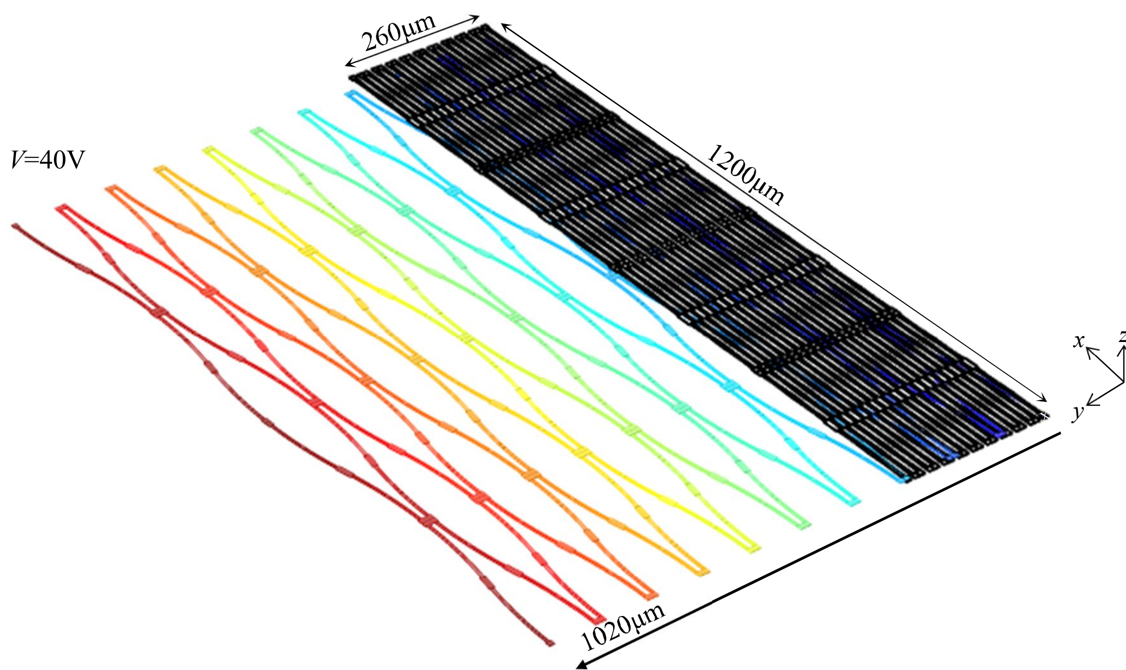

Figure 4.4: Finite element analysis simulation of a 2D array of s-drive operating in axial-mode. It is possible to nest s-drive to form a 2D array, in this array the rightmost end is anchored. Here there are 20 s-drives in *y* direction and 4 s-drives in *x* direction. Upon application of 40 V it deflects by 1020 μm which is twenty times the deflection of a s-drive. Hence in axial-mode the increase in deflection is proportional to the number s-drives in *y* direction.

Figure 4.4 shows the simulated 2D array in axial-mode. This array has 20 s-drives in *y* direction and 4 s-drives in *x* direction. Upon application of 40 V it deflects by 1020

μm which is twenty times the deflection of one s-drive. Hence in the axial-mode the increase in deflection is proportional to the number s-drives in the *y* direction.

4.2.2 Shear-Mode

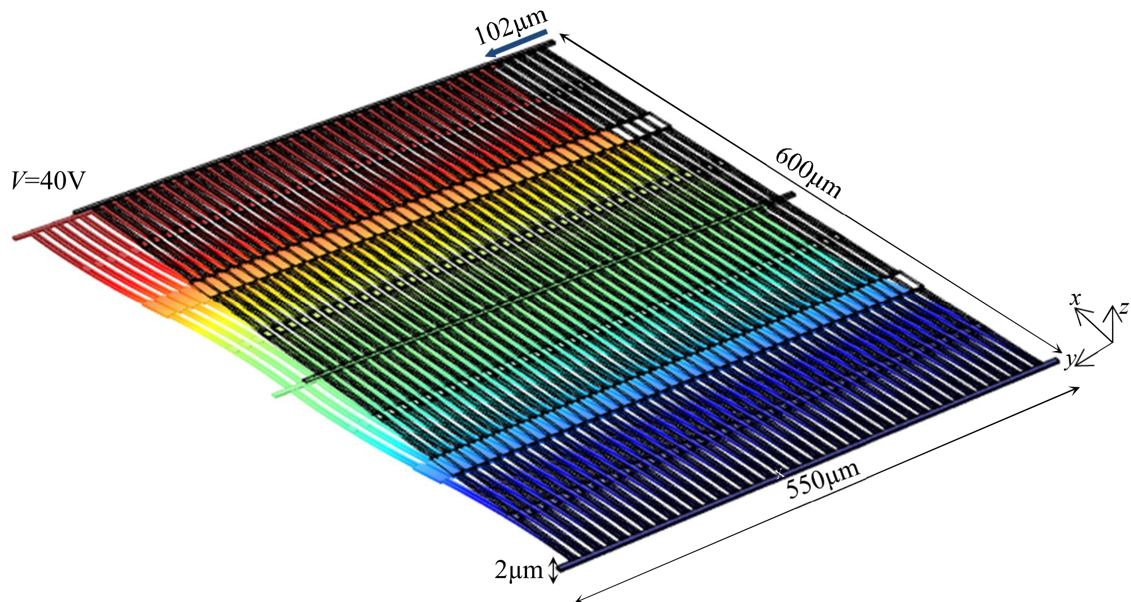

Figure 4.5: Finite element analysis simulation of a 2D array of s-drive operating in shear-mode. It is possible to nest s-drives to form a 2D array, in this array the bottom end is anchored. Here there are 40 s-drives in *y* direction and 2 s-drives in *x* direction. Upon application of 40 V it shears by 102 μm which is two times the shear of 1D array. Hence the increase in shear is proportional to the number s-drives in *x* direction.

Figure 4.5 shows the simulated 2D array in shear-mode. This array has 40 s-drives in *y* direction and 2 s-drives in *x* direction. Upon application of 40 V it deflects by 102 μm which is two times the deflection of one s-drive. Hence in shear-mode the increase in deflection is proportional to the number s-drives in *x* direction.

CHAPTER 5. EXPERIMENTAL VALIDATION OF DEVELOPED ANALYTICAL MODEL AND FEA SIMULATIONS

The s-drive [18], a new type of nestable piezoelectric micro actuator, was presented in previous chapters. This chapter presents the validation of the s-drive concept, with the experimental results from the fabricated s-drive and its nested arrays.

5.1 Fabricated S-Drive Design

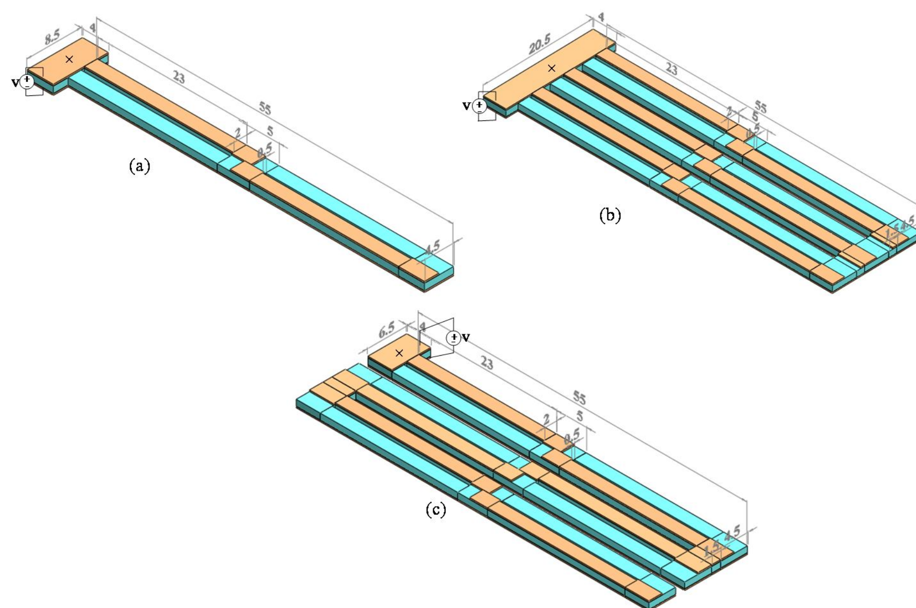

Figure 5.1: Schematic of s-drive and nested s-drive in shear-mode and axial-mode. The blue regions represent the piezoelectric material and the brown regions in the top represent the electrodes with a voltage $V=V_0$ and the brown regions in the bottom represent the electrodes at $V = 0$. (a) shows the circuit of s-drive, (b) is the circuit of nested s-drive in shear-mode and (c) is the circuit of nested s-drive in axial-mode. The '×' indicates the anchor point. All the dimensions are in mm and the thickness of the structure is $h = 0.127$ mm.

Table 5.1: Material properties of PZT5A [55].

Piezoelectric	
33 Piezoelectric strain coefficient (d_{33})	390×10^{-12} m/V
31 Piezoelectric strain coefficient (d_{31})	-190×10^{-12} m/V
Piezoelectric thickness (h)	0.127 mm
Resistivity (ρ_{PZT})	1.8×10^{2} Ωm
Relative permittivity (ε_{33}^{T})	800
Dielectric breakdown	40 V/μm
Thermal	
Curie temperature	350 °C
Mechanical	
Density	7800 kg/m^3
Elastic modulus (Y_1^p)	6.6×10^{10} N/m^2

Figure 5.1 shows the schematic of the s-drive and its nested arrays in shear-mode and axial-mode. Table 5.1 provides the material properties of PZT5A.

5.2 Simulation

The 3D piezo module of COMSOL Multiphysics 4.3a was used for the finite element analysis (FEA) simulations. The leftmost end of the s-drive was fixed, the bottom electrode was at ground and a voltage $V=V_0$ was applied on the top electrode as shown in Figure 5.1. The material properties of simulation are given in Table 5.1, and geometric properties are given in Figure 5.1. Upon application of 50 V, the s-drive deflects by 17.6 μm as shown in Figure 5.2(a), three s-drives, nested in shear-mode displace by 17.6 μm as shown in Figure 5.2(b), and three s-drives, nested in axial-mode, magnify the deflection by a factor of three as shown in Figure 5.2(c).

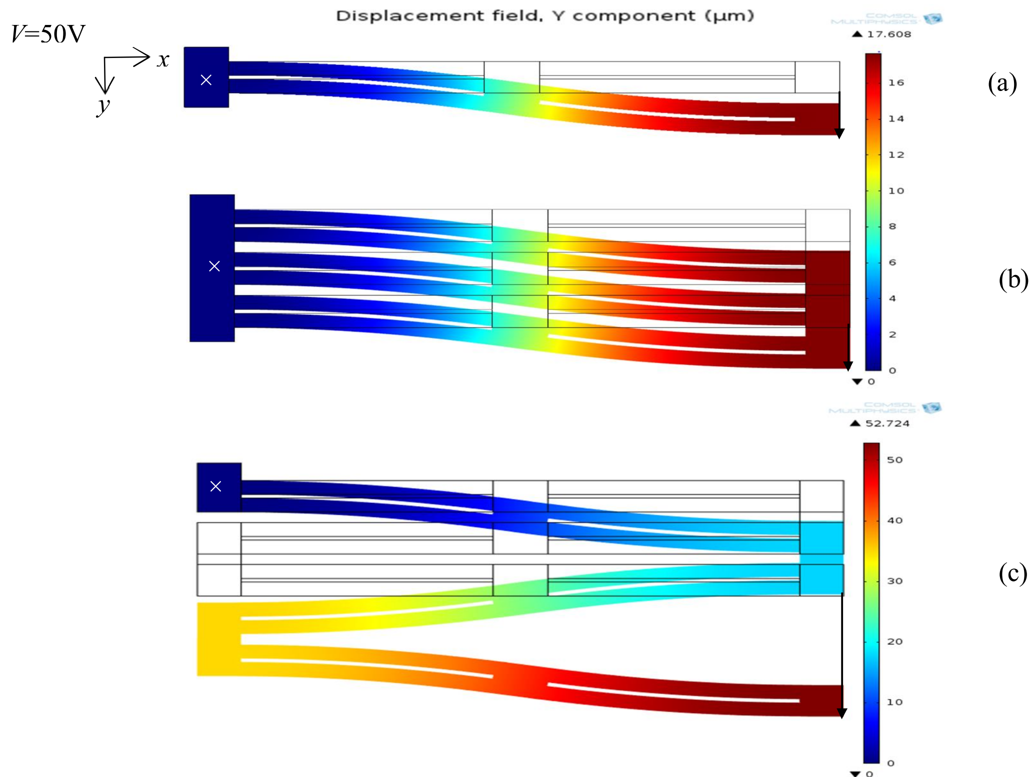

Figure 5.2: Top view of simulated s-drive and the 1D array of s-drive. The '×' indicates the anchor point and upon application of 50 V. (a) The s-drive deflects by 17.6 μm. (b) An array of three s-drives in shear mode shear by 17.6 μm. (c) Three s-drives nested in axial-mode magnify the defection by a factor of three. The material parameters of simulation are given in Table 5.1, and geometric properties are given in Figure 5.1.

5.3 Analytical Model

This section presents the analytical model for calculating the lateral displacement of the s-drive, in a configuration similar to the one fabricated. In this analysis the s-drive is divided into rectangular elements that are indicated by numbers 1 to 6 in Figure 5.3.

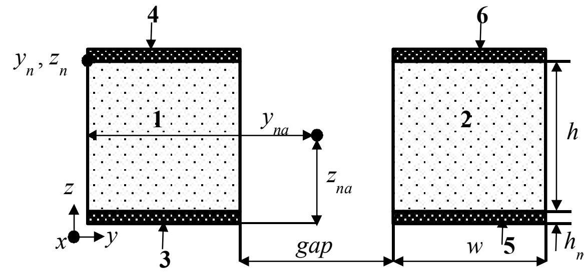

Figure 5.3: Schematic cross section of s-drive. Here piezoelectric material is sandwiched between two metal layers. The gap between the sandwiches is air. y_{na}, z_{na} correspond to the location of neutral axis from the s-drives origin. The coordinates of the nth element with reference to the s-drives origin are y_n , z_n.

For small angle approximation the curvature of s-drive due to a bending moment is given by

$$\frac{d^2y}{dx^2} = \frac{M_z}{(EI)_z}, \tag{5.1}$$

where M_z is the z-axis bending moment due to the axial stress, the flexural rigidity is $(EI)_z$, with E being the Young's modulus in the axial direction and I the second moment of area. Integration of (5.1) gives the lateral displacement of the s-drive as

$$y(x) = \frac{M_z x^2}{4(EI)_z}. \tag{5.2}$$

Derivation of moment about z-axis and flexural rigidity is given below.

Neutral axis: The neutral axis locates the radius of curvature of the actuator. If the bending moment is calculated about the neutral axis, the contribution of axial deformation can be neglected. In Figure 5.3, the neutral axis placement is shown by y_{na}, z_{na}. The location of centroid from s-drives origin can be calculated by

$$y_{na} = \frac{\sum_{elements} \iint_A E^n y dy dz}{\sum_{elements} \iint_A E^n dy dz}, \tag{5.3}$$

$$y_{na} = \frac{\sum_{elements} \int_{z_n}^{z_n+\Delta z_n} \int_{y_n}^{y_n+\Delta y_n} E^n y dy dz}{\sum_{elements} \int_{z_n}^{z_n+\Delta z_n} \int_{y_n}^{y_n+\Delta y_n} E^n dy dz}, \tag{5.4}$$

where (y_n, z_n) are the nth element coordinates from the s-drives origin (y, z), and Δy_n, Δz_n are the element width and thickness respectively, and E^n is the nth element's Young's modulus in the axial direction. A similar equation can be written for z_{na}. The schematic shown in Figure 5.3 gives

$$y_{na} = w + \frac{gap}{2}. \tag{5.5}$$

Flexural rigidity: The flexural rigidity for multilayer structure about the z-axis can be calculated from

$$(EI)_z = \sum_{elements} \int_{z_n - z_{na}}^{z_n+\Delta z_n - z_{na}} \int_{y_n - y_{na}}^{y_n+\Delta y_n - y_{na}} E^n y^2 dy dz, \tag{5.6}$$

which gives

$$(E_1 I)_z = \left(E_1^p h + 2E_1^m h_m\right) w \left\{\frac{2w^2}{3} + gap\left(w + \frac{gap}{2}\right)\right\}. \tag{5.7}$$

Bending Moment: For a multilayer structure the z-axis bending moment due to axial stress can be calculated from

$$M_z = \sum_{elements} \int_{z_n - z_{na}}^{z_n + \Delta z_n - z_{na}} \int_{y_n - y_{na}}^{y_n + \Delta y_n - y_{na}} T_1^n y dy dz . \tag{5.8}$$

where, T_1^n is the stress profile within an element. The stress in the piezoelectric element for compression is $T_1^n = E^p S_1^n - d_{31} E^p \frac{V}{h}$ [65] and for extension is $T_1^n = E^p S_1^n + d_{31} E^p \frac{V}{h}$ [65], and stress in metal layers is $T_1^n = -E^m S_1^n$ for compression and $T_1^n = +E^m S_1^n$ for extension. E^p is the piezoelectric material's Young's modulus in the axial direction, S_1^n is the axial strain in the element, d_{31} is the peizoelectric coefficient for length change in m/V, voltage applied across the piezoelectric material thickness is V, h is the piezoelectric material's thickness, and E^m is the Young's modulus of the metal layer. $S_1^n = 0$ as the bending moment is calculated with the neutral axis as the reference. Substituting the element coordinates and the stress terms in (5.8) gives

$$M_z = \frac{-w d_{31} E^p V (gap + w)}{2} . \tag{5.9}$$

Substituting (5.7) and (5.9) in (5.2) gives

$$y(L) = \frac{-d_{31} E^p V (gap + w) L^2}{8 \left(E^p h + 2 E^m h_m \right) \left\{ \frac{2w^2}{3} + gap \left(w + \frac{gap}{2} \right) \right\}} . \tag{5.10}$$

For a 1D array of 'N' number of s-drives, the displacement of the axial-mode array is given by N times $y(L)$. Where $y(L)$ is the displacement of 1 s-drive which is given by (5.10). For shear-mode array the displacement is independent of N and is given by $y(L)$.

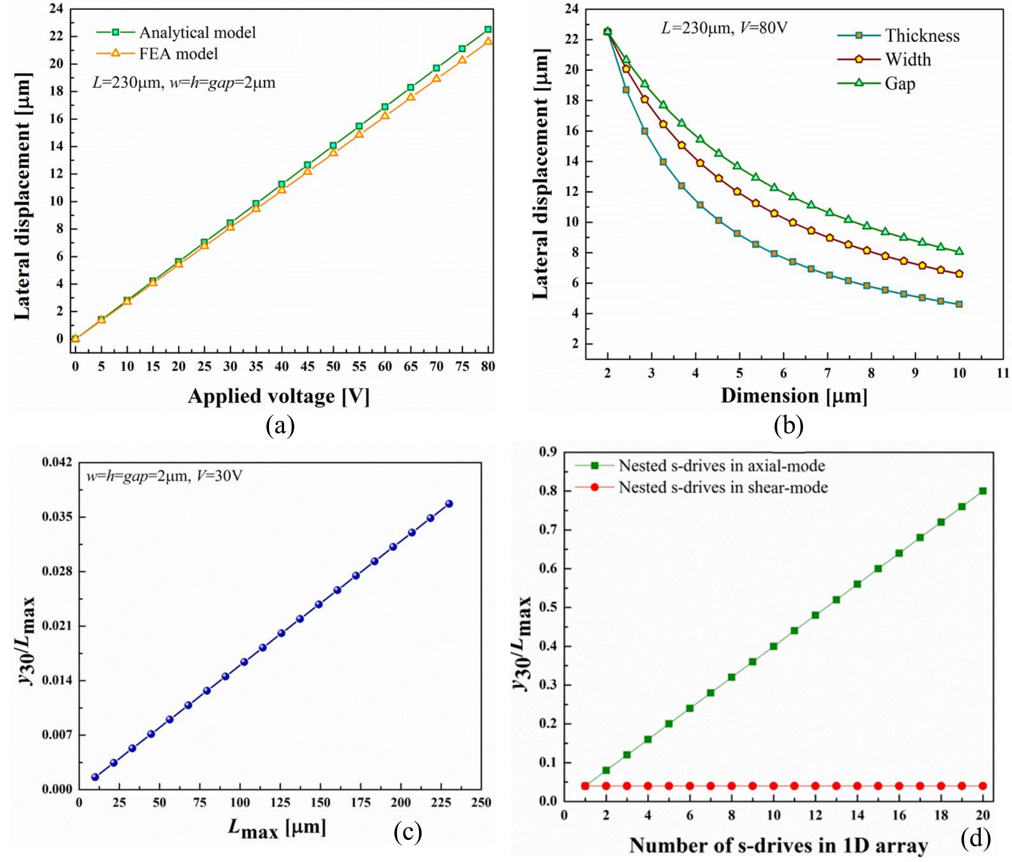

Figure 5.4: Effect of applied voltage, various dimensions and nestability on s-drive's displacement (a) shows the change in displacement with applied voltage, (b) shows the change in displacement with thickness, gap, and width, (c) shows change of $y_{30}/L_{\max}$ with $L_{\max}$ and (d) shows change of $y_{30}/L_{\max}$ for the nested s-drive arrays.

Figure 5.4 shows the change in displacement of the s-drive with applied voltage, dimensions and nestability. Figure 5.4(a) shows that the displacements predicted by analytical model compare well with the FEA model, with an average relative error of 6.5%. The difference in the method of discretization of the domain in FEA solver and in analytical model is the reason for this error. Figure 5.4(b) shows the decrease in s-drives lateral displacement due to an increase in thickness, width, or gap, independently and Figure 5.4(c) shows the increase in $y_{30}/L_{\max}$ with increase in $L_{\max}$. The reason for this is

the dependence of lateral displacement on t^{-1}, w^{-1}, h^{-1} and L^2 which can be seen in (6.10). From Figure 5.4(d), it can be seen that the $y_{30}/L_{\max}$ increases for axial-mode array with increase in the number of s-drives in the array and for shear-mode array it remains constant. The axial-mode array increases the lateral displacement proportional to the number of s-drives in the nested array and shear-mode array gives the same shear which is independent of the number of s-drives in the 1D nested array. Also, the s-drives could be nested to form a $M \times N$ 2D array to magnify the shear proportional to M.

5.4 Fabrication

During the past few decades, the ultrafast lasers have shown wide applications in high-precision micromachining [66]. Due to the ultra-short laser pulse and extremely high peak power, nonlinear absorption takes place in the working material and produce a highly-confined heating spot, inducing highly-localized ablation to remove the material, therefore it yields superior accuracy and cleanness after machining [66, 67]. The ultrafast laser machining is capable of cutting various types of materials including metals, glass, polymer, ceramics [66-69]. Also, it is well suited for micromachining of piezoelectric materials [70-72].

The piezoelectric material used for fabrication of the actuator is a poled PZT5A (T105-A4E-602) from Piezo Systems, Inc. [55]. The material has a 0.127mm thick PZT5A, with 50nm nickel electrodes. Table 6.1 provides the piezoelectric and material properties.

The s-drive and nested s-drives were fabricated from PZT5A using a focused ultrafast pulse laser machining system. The femtosecond pulse laser compared with

continuous laser has an ultrashort pulse-width and ability for providing highly confined heating [67], which is ideal for the piezoelectric material. The system used ~50 fs pulse with 80 nm spectral bandwidth (full width at half maximum) centered at 800 nm wavelength, produced by a Micra-5 Ti:Sapphire laser with Legend Elite amplifier (Coherent, USA) at a repetition rate of 5 kHz. The laser was focused by a 10x objective to ensure a large depth of field necessary for machining the thick piezoelectric material. The focused spot diameter is estimated to be ~10 μm which gives an average power density of 1.3~2.5×109 W/m^2. The piezoelectric material was mounted on a high-resolution 3-axis air bearing stage (ABL1000, Aerotech) and the cutting speed was 0.2 mm/s for machining and 0.5 mm/s for electrical disconnects. The fabricated s-drive and its arrays are shown in Figure 5.5.

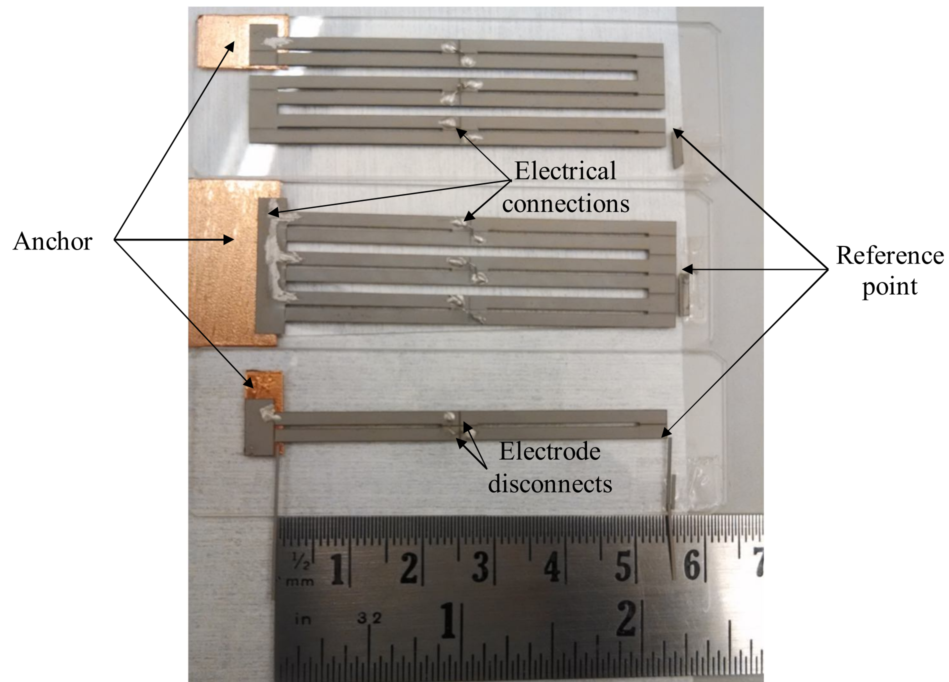

Figure 5.5: Fabricated piezoelectric actuators. Laser-machined nested s-drives in an axial-mode (top), nested s-drives in a shear-mode (center) and s-drive (bottom) with electrode disconnects, electrical connections and reference point for measurements.

5.5 Experimental Setup

The fabricated s-drive and its nested arrays were actuated at various voltages in the range of 0-50 V, with experimental measurements of displacements. These experimental measurements validated the FEA simulations methodology for both the s-drive and its nested arrays. A DC power supply 2410C by Keithley (Cleveland, OH, USA) was used for application of voltage and the setup was built under an Olympus microscope connected to a PC, for measurement of displacements, as shown in Figure 5.6.

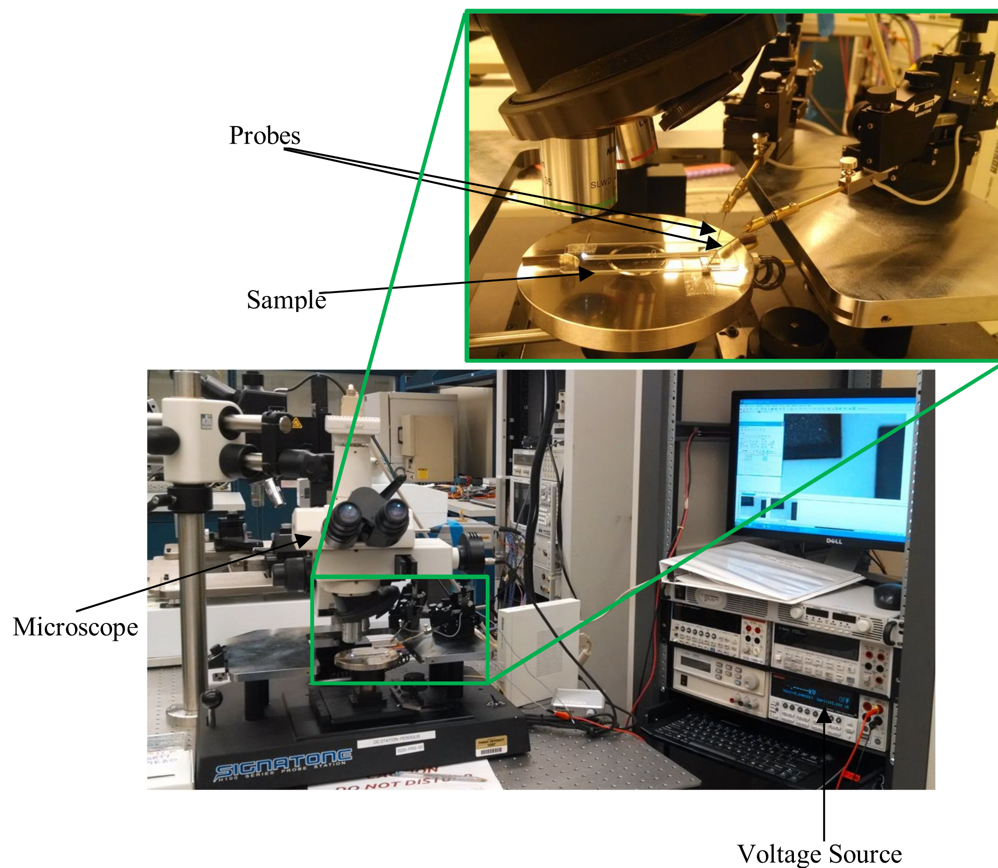

Figure 5.6: Experimental set up. The setup with two probes, voltage source for actuation and microscope with PC for measurements.

The lateral displacement of the actuator was measured by measuring the displacement of the actuator's tip with respect to the reference point as shown in Figure 5.7. In order to avoid charge accumulation, after every measurement the voltage was set back to 0 V and after the actuator returned to the original reference point, waited for about 15 minutes, the voltage was increased to the next value. Using this procedure, four repeats of measurements were completed. The average value, along with standard deviation error, of these measurements is plotted in Figure 5.8.

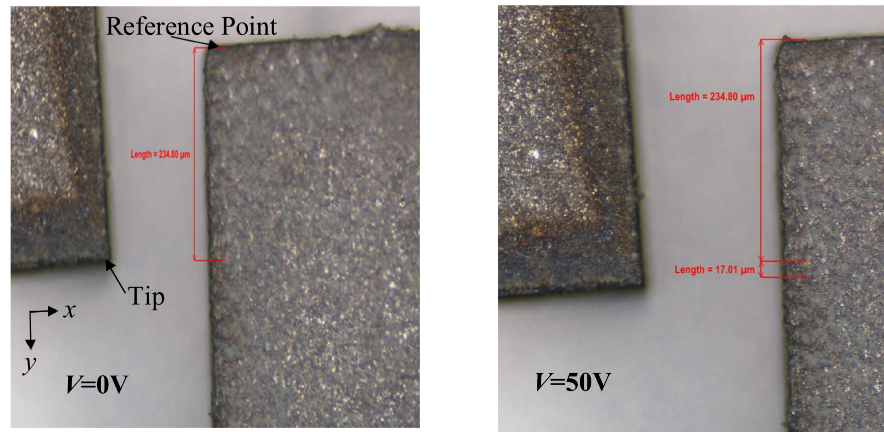

Figure 5.7: S-drive tip upon actuation. The position of the tip of s-drive before and after actuation. Upon application of 50 V, the s-drive deflects by 17.01 µm.

5.6 Experimental Results

The displacements at five different voltages were measured by following the procedure described in the previous section. As shown in Figure 5.8 the simulated displacement of s-drive and 1D nested arrays of s-drive agree well with the experimental measurements and analytical model with an average relative error of 6.3% in the 0-50 V range. The difference in analytical and FEA model is due to the method of discretization

used in these two methods. The analytical model divides the structure into six elements of rectangular cross section and the FEA model discretized the structure into thirty thousand elements.

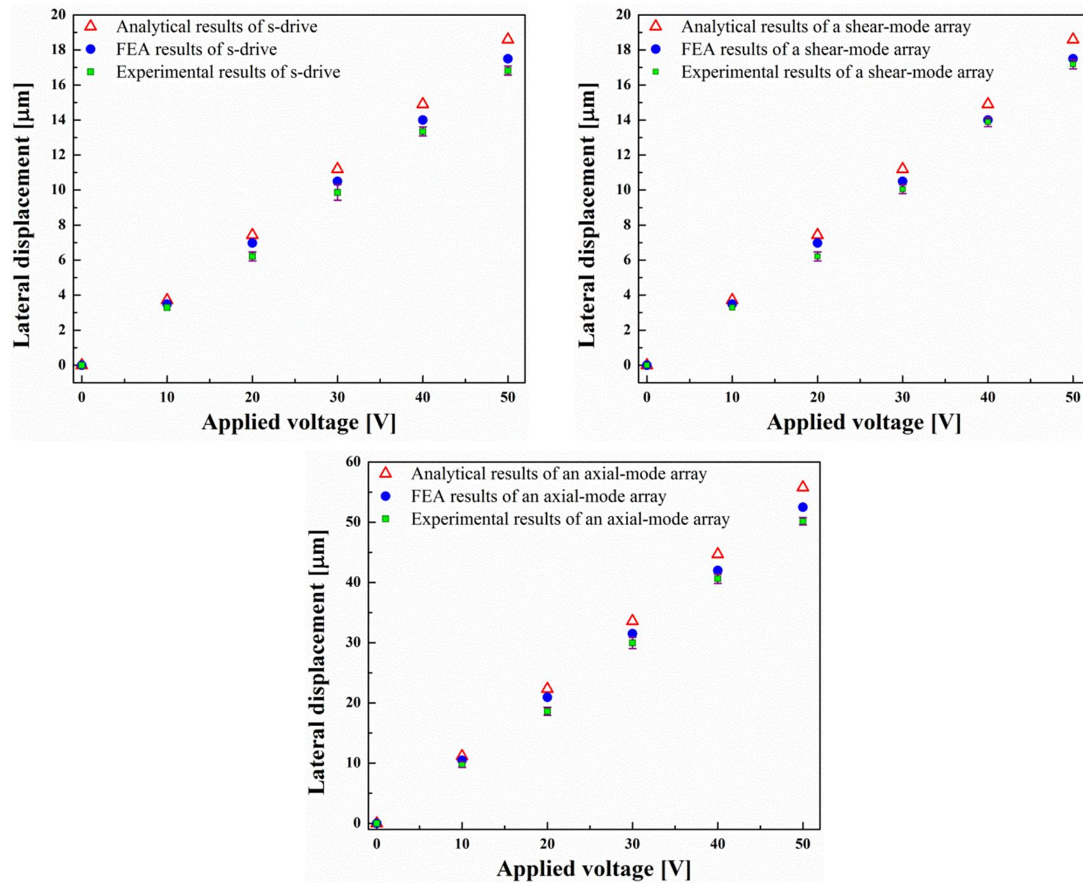

Figure 5.8: Lateral displacement versus applied voltage. The simulated results of s-drive and 1D arrays of s-drive compare well with the experimental measurements and analytical results with an average relative error of 6.3% in the range of 0-50 V.

The experimental results depend on the electrical connections, electrical disconnects, and dimensions of the structure. The dimensions of the fabricated structures will not be the same as the one used for FEA model and analytical model. There might be an uncertainty in these dimensions. Figure 5.4 shows the effect of various dimensions on the displacement of the s-drive. Also, the analytical model and FEA model neglect the

dielectric loss and hence the displacements predicted by them are slightly higher than those measured experimentally. Overall, these experimental results of s-drive and its nested arrays validate both the FEA model and the developed analytical model.

Table 5.2: Experimental displacements along with displacements calculated using analytical model and FEA model.

S-drive				
Applied voltage [V]	Analytical displacement [μm]	FEA displacement [μm]	Average experimental displacement [μm]	Experimental error [%]
0	0	0	0	0
10	3.72	3.49	3.29	0
20	7.44	6.98	6.21	0.6
30	11.2	10.5	9.87	0.4
40	14.9	14	13.35	0.2
50	18.6	17.5	16.83	0.1
S-drives nested in a shear-mode array				
Applied voltage [V]	Analytical displacement [μm]	FEA displacement [μm]	Average experimental displacement [μm]	Experimental error [%]
0	0	0	0	0
10	3.72	3.49	3.29	0
20	7.44	6.98	6.21	4
30	11.2	10.5	10.05	2.5
40	14.9	14	13.89	2
50	18.6	17.5	17.19	1.5
S-drives nested in an axial-mode array				
Applied voltage [V]	Analytical displacement [μm]	FEA displacement [μm]	Average experimental displacement [μm]	Experimental error [%]
0	0	0	0	0
10	11.16	10.47	9.77	4.8
20	22.32	20.94	18.61	3.6
30	33.6	31.5	29.98	3.2
40	44.7	42	40.62	2
50	55.8	52.5	50.18	1.2

5.7 Time for Charging and Discharging

The time for charging and discharging the s-drive can be calculated from the time constant τ. The time constant is calculated by taking the product of resistance *R* and capacitance *C*. A multimeter was used for measuring the resistance and capacitance of the s-drive. For these measurements one probe was attached to the ground terminal and the other probe was attached to the terminal where voltage is applied. For the laser machined s-drive that is shown in Figure 5.5 the multimeter measured C = 8nF and R = 124Ω and the results were repeatable. The analytical expressions for calculating these are given below. The metal electrodes and piezoelectric material are in series and net resistance of s-drive is given by (5.12).

$$C = \frac{wL\left(\varepsilon_0 \varepsilon_{33}^T + d_{31}^2 E_1^P\right)}{h}, \tag{5.11}$$

$$R = \frac{2\rho_{cu} h_m}{Lw} + \frac{2\rho_{PZT} h}{L\left(2w - gap\right)}. \tag{5.12}$$

The dimensions are given in Figure 5.3 and the piezoelectric material properties are given in Table 5.1. The other parameters are permittivity of free space $\varepsilon_0 = 8.854\times10^{-12}$ F/m, resistivity of copper $\rho_{cu} = 1.72\times10^{-8}$ Ωm [54]. Substituting these values give R = 118.7 Ω and C = 8.402 nF. The values have a relative error of 4% with respect to the experimental results.

From the measured values of R and C the time constant is 1 μsec. Hence, the s-drive comes back to its original state almost instantaneously and the fifteen minutes duration was the time I waited between measurements.

5.8 Measured Displacements while Switching from $+V_0$ to $-V_0$

The s-drives tip displacement was measured by switching the voltage between positive and negative voltages. Two sets of measurements were taken and the average value of displacement is ±3.39 μm depending on the voltage polarity. Figure 5.9 shows tip deflection upon application of voltage.

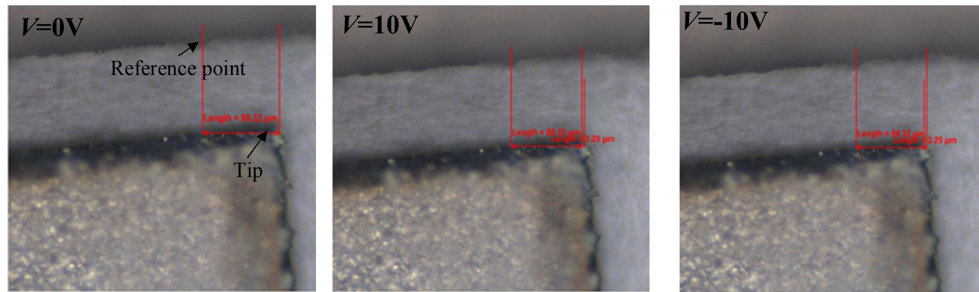

Figure 5.9: S-drive tip upon actuation. The position of the tip of s-drive before and after actuation between +10 V and -10 V. The s-drive deflects by ±3.29 μm.

Table 5.3: Displacement of s-drive while switching between $+V_0$ to $-V_0$.

Applied voltage [V]	Analytical displacement [μm]	FEA displacement [μm]	Average experimental displacement [μm]
0	0	0	0
10	3.72	3.49	3.39
-10	-3.72	3.49	-3.39

5.9 Microfabrication

The piezoelectric material used for fabrication of the actuator is a poled PVDF (1003702-7) from Measurement Specialties [56].The material has a 9 μm thick PVDF, with 60 nm copper electrodes. Table 5.4 provides the piezoelectric and material properties. The s-drive was fabricated from PVDF using focused ion beam (FIB) etching. In FIB gallium ions strike the PVDF to remove material in the form of secondary ions

and atoms. The steps followed for the fabrication of a 100 μm s-drive are shown in Figure 5.10. But the actuator's tip broke before actuation while transferring the sample from the stub (used for mounting sample for FIB) to a glass slide for actuation. In order to avoid this, in the future the sample should be mounted on the glass slide or silicon wafer even before etching.

Table 5.4: Material properties of PVDF [56].

Piezoelectric	
33 Piezoelectric strain coefficient (d_{33})	26×10^{-12}m/V
31 Piezoelectric strain coefficient (d_{31})	-21×10^{-12}m/V
Piezoelectric thickness (h)	9 μm
Dielectric breakdown	80 V/μm
Thermal	
Curie temperature	103 °C
Mechanical	
Density	1780 kg/m^3
Elastic modulus (Y_1^p)	7.7×10^8 N/m^2

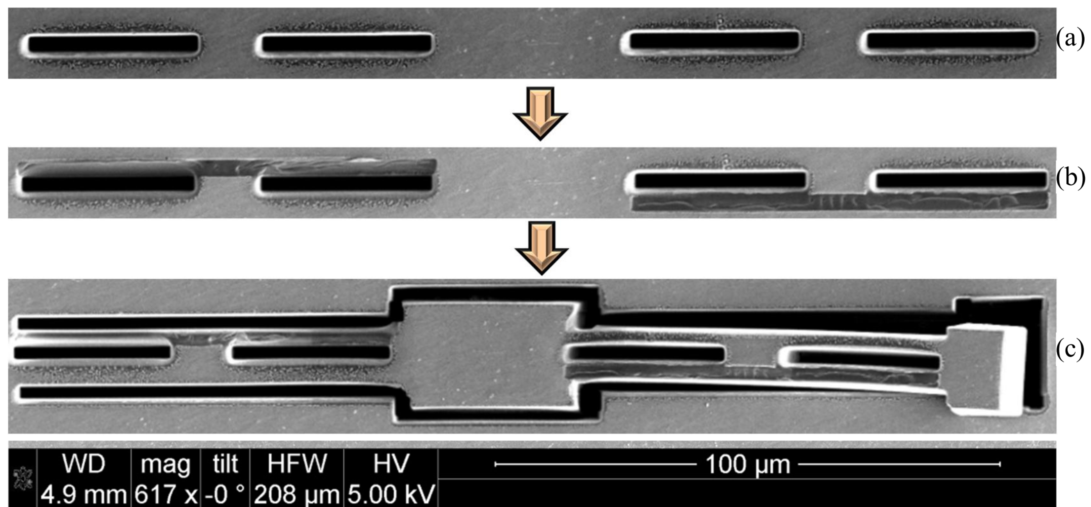

Figure 5.10: Fabrication steps: (a) shows the cutting of central holes, (b) shows the removal of electrode layers, and (c) shows the cutting of through holes to make the s-drive.

CHAPTER 6. POSSIBLE APPLICATIONS OF NESTED S-DRIVES

This chapter explores the possible applications of nested s-drives to function as an s-drive [18] probe or channel flow piezo pen. In the proposed design, two sets of nested s-drives in shear-mode are placed orthogonal to each other to achieve two degrees of freedom. An addition of out-of-plane piezo stack to the proposed design could provide the third degree of freedom. This chapter also reviews the existing dip pen nanolithography (DPN) technology with some of its advantages and applications. The proposed design could work as a new type of DPN. The channel flow piezo pen is able to produce large deflections, with multiple degrees of freedom, and might handle multiple inks with the capability of writing on many surfaces in either wet or dry, clean or dirty environments.

6.1 Dip Pen Nanolithography

Dip pen nanolithography (DPN) is a scanning probe based tool that plays an important role in patterning various types of materials on a substrate. This tool is easily accessible for researchers with access to an atomic force microscope. For microfabrication, nanotechnology, and molecular electronics, lithographic method plays an important role. The technique used in dip pen technology is approximately 4000 years

old. Where, ink is transported to via a sharp object to a surface due to capillary forces [73]. Mirkin's group in 1999 reported a new type of dip pen nanolithography (DPN) [74] where the molecules with chemical affinity (ink) to a solid-state substrate (paper) were deposited from an atomic force microscope (AFM) tip (nib). In short DPN can be defined as a direct-write scanning probe-based lithography [75].

6.1.1 Advantages of DPN

Some advantages of DPN are [74-76]:

- This is a direct-write constructive lithographic tool that allows deposition of both soft and hard materials [76].
- Any premodification of the surface is not required and cross contamination can be prevented [76].
- This technique can deposit multiple compounds in series or in parallel [74-76].

6.1.2 Types of DPN

DPN is the only lithography technique that offers the capability of direct printing with high resolution and registration [77]. This tool is specifically useful for patterning of biological structures onto the substrates. All the depositions are possible without exposing the substrate to harsh conditions.

- Electrochemical DPN (E-DPN) [78, 79] an AFM lithography technique which depends on spontaneous condensation that causes the transport of material from the AFM tip to the surface [76].
- Lee *et al*. in [80] screened human immunodeficiency HIV-1virus by using nanoarrays of anti-p24 antibody.
- Coffey *et al*. in [81] used DPN as a rapid prototyping tool to generate and study nanoscale structures in thin composite polymer films [76].
- *Thermal DPN:* Sheehan and co-workers in [82] demonstrated the direct deposition of continuous indium lines onto glass or silicon surfaces, by thermally heating the tip. In this technique the change in tip temperature can control the rate of ink deposition.
- *Electropen nanolithography:* Cai et al. in [83] presented the electropen nanolithography (EPN), in this technique the ink material from the tip was coupled to the substrate through electrochemical modification.
- *Modified AFM:* Wang *et al.* [84], Zhang *et al.*[85], Zou *et al.*[86], have shown the fabrication of AFM tips from poly(dimethylsiloxane) (PDMS)for increasing the ink carrying capacity.
- *Nanofountain pen:* Espinosa *et al.* [87] fabricated the ‘nanofountain pen’ (NFP) where microfluidic channels were included in the AFM cantilevers. These channels ensured a constant supply of ink.

In the existing DPN technology, pens might handle only one type of ink, work in only clean and dry environment, and have a moving substrate. In the following section we describe a new type of DPN that is capable of resolving these problems.

6.2 Nested S-Drive Design

This section provides a detailed description of the basic design of the nested s-drives that can function as a new type of DPN or probe. In order to function as a new type of DPN known as channel flow piezo pen, channels need to be incorporated into the s-drives.

6.2.1 Pen/Probe Design

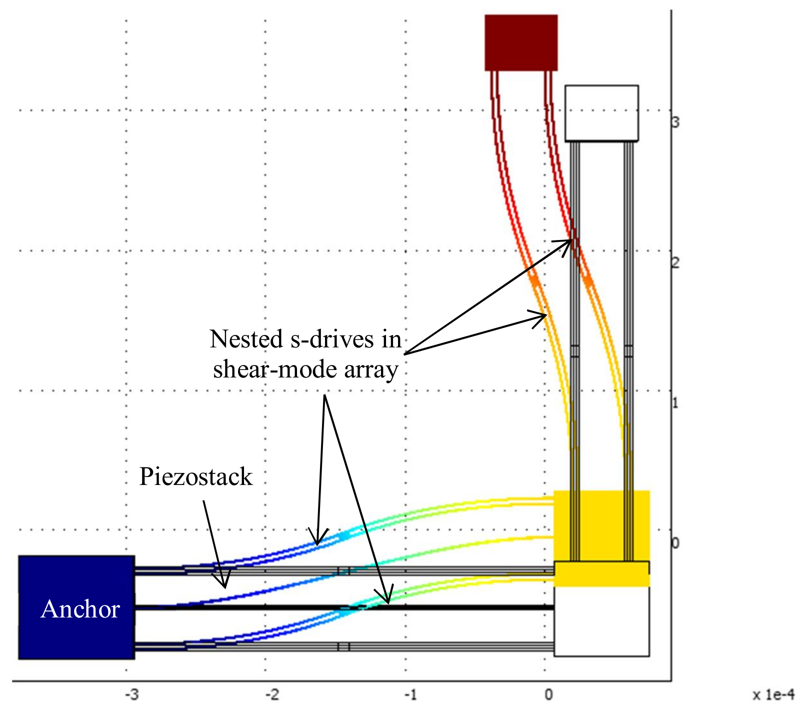

Figure 6.1: The basic design of nested s-drives to function as a new type of DPN or a probe. In this design, two pairs of arrays of s-drives in shear-mode are placed orthogonal to achieve the in-plane x, y movements and the piezostack achieves the out-of-plane movement in z direction.

The basic design of the pen is shown in Figure 6.1. It consists of two nested s-drives in shear-mode and a piezostack. The shear-mode arrays are orthogonal to each

other. These arrays provide the in-plane x, y movement and the piezostack provides the out-of-plane z movement.

6.2.2 Electrode Connections

The required electrode connections are shown in Figure 6.2. Using such connections it is possible to control the shear-mode arrays independently. For example consider a situation where the both the arrays have a voltage of 40 V being applied. Now if we want to apply 50 V to array providing x movement but have the array providing y movement at 40 V, all we need to do is increase the voltage of top and bottom electrodes of y movement array by 10 V. So, now because of the wiring shown in Figure 6.2, the voltage applied across y movement array is 40 V and that across x movement array is 50 V.

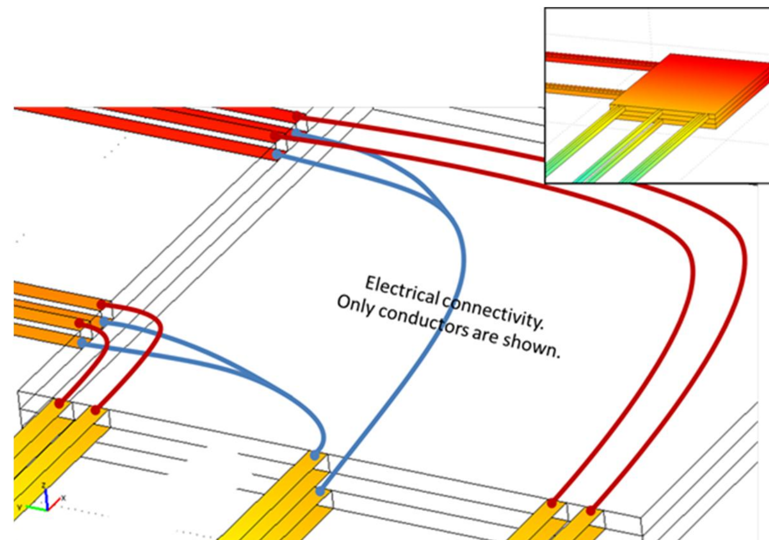

Figure 6.2: Wiring for independent control of nested shear-mode arrays of s-drives.

6.2.3 One Complete Cycle for In-Plane Movement

This section presents the simulation results of one complete cycle of the Pen/Probe design. In COMSOL upon application of 40 V the pen displaces by 52 µm in x and y directions as shown in the following figures.

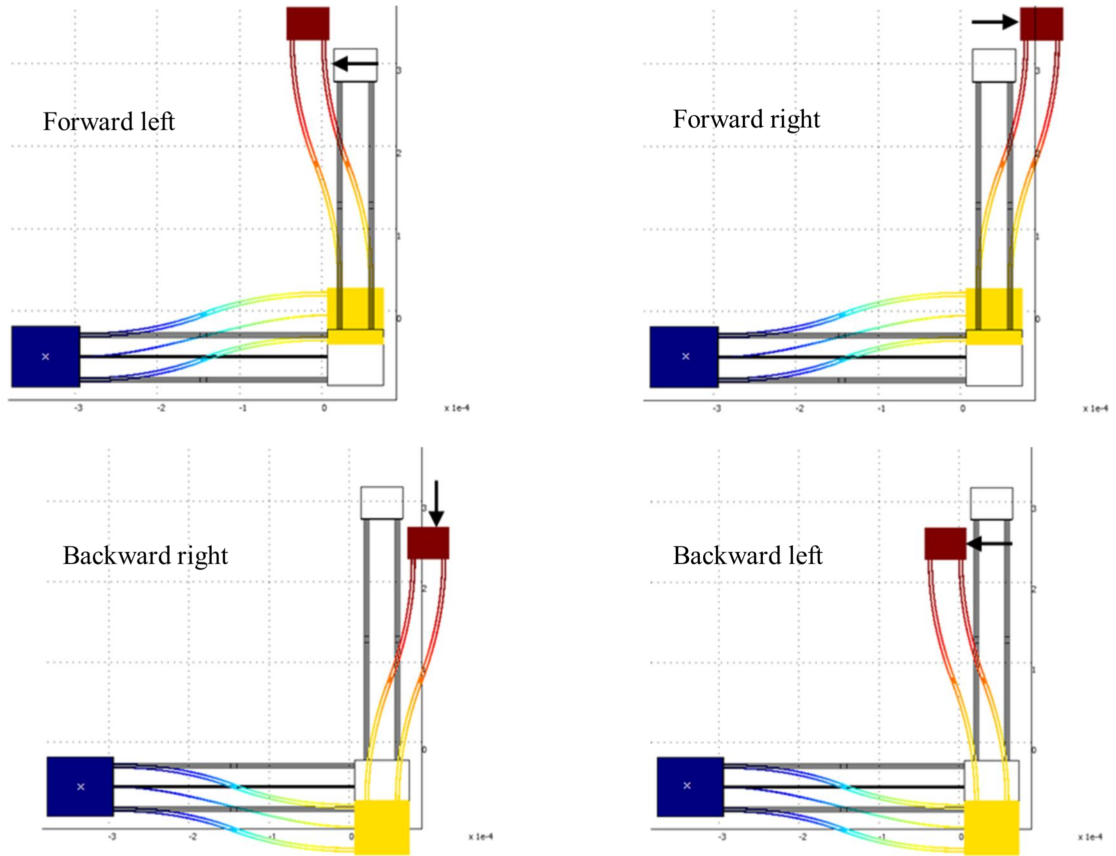

Figure 6.3: In-plane movement of pen/probe. The figure shows the movement in the forward left direction, right direction, backward right direction, left direction

6.2.4 Out-of-Plane Movement

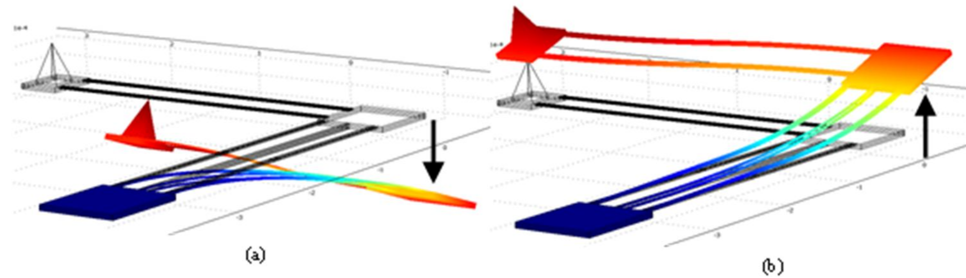

Figure 6.4: Out-of-plane movement of pen/probe. (a) shows the downward movement and (b) shows the upward movement.

The piezoelectric stack provides the out-of-plane movement. Figure 6.4(a), (b) show the movement in *z*-direction.

6.2.5 Possible Fabrication Steps

The possible nine steps needed for fabricating the channel flow piezo pen are given in this section. Fabricating this device, in the future, will help in validating the multiple degrees of freedom concept of s-drive.

Step 1: Start with the Si substrate.

Step 2: Deposit AZ1518 photoresist.

Step 3: The lower conductor is deposited through sputtering.

Step 4: Spin photo resist for creating channels.

Step 5: Piezoelectric gel is spun and hardened.

Step 6: The upper conductor layer is deposited.

Step 7: Deposition of LPCVD oxide and pattern with photo resist.

Step 8: Removal of photoresist from the channels.

Step 9: Dry etching and dry release of the device.

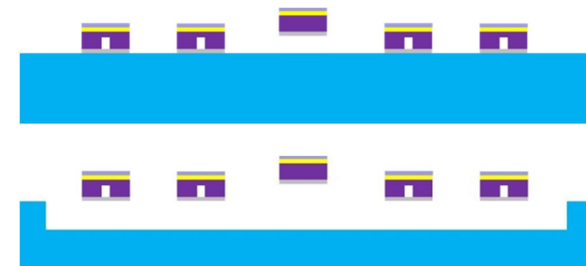

6.3 Summary of S-drive Pen/Probe

Table 6.1: Channel flow piezo pen versus conventional dip pen.

Channel flow piezo pen	Conventional dip pen
Pen can move in *x*, *y*, *z* directions	Moving substrate
Write on many surface	Piezo stage
Could achieve continuous writing	Cannot achieve continuous writing, as it does not have continuous ink supply
Wet/dry, clean/dirty environment	Clean and dirty environment

Table 6.2: S-drive probe versus conventional probe.

Feature	S-drive probe	Conventional probe
Increase scan rate	Yes	No
Position feedback	Yes	No
Calibrate due to feedback	Yes	No
Requires laser position feedback	No	Yes

CHAPTER 7. SUMMARY AND FUTURE DIRECTION

7.1 Summary

Nestable actuators may find applications in robotics, scanning probe microscopy, lithography, micro-scale assembly and nano-scale assembly [18]. Due to the small strain limits of piezoelectric materials, most of the existing piezoelectric actuators have relatively small deflections. A novel nestable piezoelectric microactuator called the s-drive that is geometrically configured to magnify the small piezoelectric strains into larger deflections has been presented. In the s-drive actuator, the piezoelectric material is sandwiched between two conductors, and the electrodes are configured such that an application of voltage causes an extension on two beams and compression on the other two beams to produce a large lateral deflection in the form of an 's' shape [18]. The s-drive gets its name from the characteristic 's' shape that appears upon actuation.

The four possible configurations of s-drive were shown and the possible 1D and 2D arrays of s-drive in axial-mode and shear-mode for magnification of displacement and shear were presented. The effect of scaling the s-drive in three dimensions was analyzed. The ratio of lateral displacement to length of s-drive decreased as the scaling increased. Hence, it is better to have smaller s-drives.

An analytical model for calculating the lateral displacement and stiffness of the s-drive was developed. The developed analytical model predicts displacement close to the displacement of finite element analysis model with average relative error of 6%. Since, the analytical model is valid only in the linear regime, it consistently predicts higher deflections than the FEA model. The developed analytical model was used to understand the variation of displacement of the s-drive with applied voltage, dimensions and nestability.

The experimental results validated the FEA model and the developed analytical model for s-drive and its nested arrays. The s-drive, its shear-mode and axial-mode nested arrays were fabricated from PZT5A using the focused ultrafast pulse laser machining system. The FEA simulation agrees well with the experimental measurements and analytical model with an average relative error of 6.3% (0-50 V). Future work proposed includes microfabrication of s-drive and its nested arrays.

Achieving multiple degrees of freedom with the s-drive was explored and the design for nested s-drives to function as microscale probe or function as a channel flow piezo pen was proposed. Compared to the conventional nanolithography the piezo pen has large deflection with multiple degrees of freedom, and can write on any surface, in any environment.

Overall, in this dissertation, the concept of a novel, nestable, large displacement, piezoelectric microactuator was introduced and the experimental results validated the FEA model and the developed analytical model for s-drive and its nested arrays. We have also proposed a possible application of nested s-drives to function as microscale probe or channel flow piezo pen.

7.2 Future Direction

Some of the possible future directions of s-drive and its nested arrays could be in biological applications, energy harvesting applications, variable diffraction gratings, variable filtering, scanning probe microscopy, nanolithography and micro-assembly [18].

The fabrication of these actuators at the microscale will help in exploring more applications and modifications of the actuators. As mentioned in Chapter 5 an attempt for fabrication of s-drive in microscale from PVDF was made. This method was time consuming (>12 hrs) and the s-drives tip broke even before the actuation. Hence to avoid any damage to the actuator, it would be better to mount the sample on a silicon wafer or glass slide before the fabrication. This type of mounting would help in easier actuation. Also in order to reduce the fabrication time it will useful to explore other fabrication methods such as chemical etching, electron lithography, and CNC milling.

LIST OF REFERENCES

LIST OF REFERENCES

[1] C. Li and C. D. Rahn, "Design of Continuous Backbone, Cable-Driven Robots," *Journal of Mechanical Design,* vol. 124, pp. 265-271, 2002.

[2] W. K. Jeung, Y. J. Kim, and S. M. Choi, "Large Displacement Out-Of-Plane Bimorph Actuator for Optical Application," *Key Engineering Materials*, pp. 1383-1386, 2006.

[3] L. Wu and H. Xie, "A Large Vertical Displacement Electrothermal Bimorph Microactuator with Very Small Lateral Shift," *Sensors and Actuators A: Physical,* vol. 145–146, pp. 371–379, 2008.

[4] J. Kwon, J. Hong, Y. S. Kim, D. Y. Lee, K. Lee, S. M. Lee and S. I. Park, "Atomic Force Microscope with Improved Scan Accuracy, Scan Speed, and Optical Vision," *Review of Scientific Instruments*, vol. 74, pp.4378-4383,2003.

[5] P. J. Gilgunn, L. Jingwei, N. Sarkar, and G. K. Fedder, "CMOS-MEMS Lateral Electrothermal Actuators," *Journal of Microelectromechanical Systems*, vol. 17, pp. 103-114, 2008.

[6] Q. Long, P. J. Sung, and Y. B. Gianchandani, "Bent-Beam Electrothermal Actuators-Part I: Single Beam and Cascaded Devices," *Journal of Microelectromechanical Systems*, vol. 10, pp. 247-254, 2001.

[7] Q. A. Huang and N. K. S. Lee, "Analysis and Design of Polysilicon Thermal Flexure Actuator," *Journal of Microelectromechanical Systems*, vol. 9, pp. 64-70, 1999.

[8] R. Legtenberg, A. W. Groeneveld, and M. Elwenspoek, "Comb-Drive Actuators for Large Displacements," *Journal of Micromechanics and microengineering,* vol. 6, pp. 320-329, 1996.

[9] M. Potter, K. Gouder, and J. F. Morrison, "A Numerical Model for Electro-Active Polymer Actuators with Experimental Validation," *Sensors and Actuators A: Physical,* vol. 170, pp. 121-130, 2011.

[10] H. K. R. Kommepalli, H. G. Yu, C. L. Muhlstein, S. Trolier-McKinstry, C. D. Rahn, and S. A. Tadigadapa, "Design, Fabrication, and Performance of a Piezoelectric Uniflex Microactuator," *Journal of Microelectromechanical Systems,* vol. 18, pp. 616-625, 2009.

[11] Z. Yong, S. O. R. Moheimani, and M. R. Yuce, "Bidirectional Electrothermal Actuator With Z-Shaped Beams," *IEEE Sensors Journal*, vol. 12, pp. 2508-2509, 2012.

[12] H. Fujita and K. J. Gabriel, "New Opportunities for Microactuators," *Solid-State Sensors and Actuators*, pp. 14-20, 1991.

[13] Y. B. Cohen, "Electroactive Polymers as Artificial Muscles: Capabilities, Potentials and Challenges," *Robotics*, pp. 188-196, 2000.

[14] A. Vinogradov, J. Su, C. Jenkins, and Y. B. Cohen, "State-of-the-Art Developments in the Field of Electroactive Polymers," *MRS Online Proceedings Library,* vol. 889, pp. 1-7, 2005.

[15] J. C. Nicholas, Z. J. Traina, S. G. Kim, "A Strain Amplifying Piezoelectric MEMS Actuator," *Journal of Micromechanics and Microengineering,* vol. 17, p. 781-787, 2007.

[16] X. Shen, X. Wang, and I. Lee, "Experimental Study on RAINBOW Actuators made of PSZT," *Journal of Intelligent Material Systems and Structures,* vol. 17, pp. 691-694, 2006.

[17] C. H. Cheng and S. L. Tu, "Fabrication of A Novel Piezoelectric Actuator with High Load-Bearing Capability," *Sensors and Actuators A: Physical,* vol. 141, pp. 160-165, 2008.

[18] A. Chigullapalli and J. V. Clark, "Extremely Large Deflection Actuators for Translation or Rotation," *ASME International Mechanical Engineering Congress and Exposition***,**Houston, Texas, USA,, 2012, pp. 167-173.

[19] C. Bolzmacher, K. Bauer, U. Schmid, M. Hafez, and H. Seidel, "Displacement Amplification of Piezoelectric Microactuators with a Micromachined Leverage Unit," *Sensors and Actuators A: Physical,* vol. 157, pp. 61-67, 2010.

[20] D. L. D. Voe and A. P. Pisano, "Modeling and Optimal Design of Piezoelectric Cantilever Microactuators," *Journal of Microelectromechanical Systems*, vol. 6, pp. 266-270, 1997.

[21] Z. Wang, W. Zhu, C. Zhao, and X. Yao, "Deflection Characteristics of a Trapezoidal Multilayer In-Plane Bending Piezoelectric Actuator," *IEEE Transactions Ultrason Ferroelectric Frequency Control,* vol. 48, pp. 1103-1110, 2001.

[22] Y. Hishinuma and Y. E. Hyeok, "Piezoelectric Unimorph Microactuator Arrays for Single-Crystal Silicon Continuous-Membrane Deformable Mirror," *Journal of Microelectromechanical Systems*, vol. 15, pp. 370-379, 2006.

[23] E. H. Hong, S. T. McKinstry, R. L. Smith, S. V. Krishnaswamy, and C. B. Freidhoff, "Design of MEMS PZT Circular Diaphragm Actuators to Generate Large Deflections," *Journal of Microelectromechanical Systems*, vol. 15, pp. 832-839, 2006.

[24] Y. E. Hyeok, Y. Hishinuma, C. J. Gong, S. T. McKinstry, E. Bloemhof, and B. M. Levine, "Thin-Film Piezoelectric Unimorph Actuator-Based Deformable Mirror With a Transferred Silicon Membrane," *Journal of Microelectromechanical Systems ,* vol. 15, pp. 1214-1225, 2006.

[25] M. Deshpande and L. Saggere, "An Analytical Model and Working Equations for Static Deflections of a Circular Multi-Layered Diaphragm-Type Piezoelectric Actuator," *Sensors and Actuators A: Physical,* vol. 136, pp. 673-689, 2007.

[26] S. M. Lee, S. H. Jun, C. S. Park, H. E. Kim, and K. W. Lee, "Spiral-Shaped Piezoelectric Actuator Fabricated using Thermoplastic Co-Extrusion Process," *Sensors and Actuators A: Physical,* vol. 148, pp. 245-249, 2008.

[27] O. J. Myers, M. Anjanappa, and C. B. Freidhoff, "Numerical Modeling of a Circularly Interdigitated Piezoelectric Microactuator," *Journal of Microelectromechanical Systems*, vol. 19, pp. 1098-1104, 2010.

[28] Y. Yin, H. Ye, W. Zhan, L. Hong, H. Ma, and J. Xu, "Preparation and Characterization of Unimorph Actuators Based on Piezoelectric $Pb(Zr_{0.52}Ti_{0.48})O_3$ Materials," *Sensors and Actuators A: Physical,* vol. 171, pp. 332-339, 2011.

[29] T. Yeom, T. W. Simon, M. Zhang, M. T. North, and T. Cui, "High Frequency, Large Displacement, and Low Power Consumption Piezoelectric Translational Actuator Based on an Oval Loop Shell," *Sensors and Actuators A: Physical,* vol. 176, pp. 99-109, 2012.

[30] W. Liu, Y. Zhu, K. Jia, W. Liao, Y. Tang, B. Wang, "A Tip–Tilt–Piston Micromirror with a Double S-Shaped Unimorph Piezoelectric Actuator," *Sensors and Actuators A: Physical*, vol. 193, pp. 121-128, 2013.

[31] G. H. Haertling, "Chemically Reduced Plzt Ceramics for Ultra-High Displacement Actuators," *Ferroelectrics,* vol. 154, pp. 101-106, 1994.

[32] J. Juuti, K. Kordás, R. Lonnakko, V. P. Moilanen, and S. Leppävuori, "Mechanically Amplified Large Displacement Piezoelectric Actuators," *Sensors and Actuators A: Physical,* vol. 120, pp. 225-231, 2005.

[33] H. Q. Li, D. C. Roberts, J. L. Steyn, K. T. Turner, O. Yaglioglu, N. W. Hagood, "Fabrication of a High Frequency Piezoelectric Microvalve," *Sensors and Actuators A: Physical,* vol. 111, pp. 51-56, 2004.

[34] J. G. Bonito, M. J. Brennan, S. J. Elliott, A. David, and R. J. Pinnington, "A Novel High-Displacement Piezoelectric Actuator for Active Vibration Control," *Smart Materials and Structures,* vol. 7, p. 31-42, 1998.

[35] P. Kallio, M. Lind, H. Kojola, Z. Quan, and H. N. Koivo, "An Actuation System for Parallel Link Micromanipulators," *Intelligent Robots and Systems* , vol.2., pp. 856-862, 1996.

[36] J. H. Kim, S. H. Kim, and Y. K. Kwak, "Development of a Piezoelectric Actuator using a Three-Dimensional Bridge-Type Hinge Mechanism," *Review of Scientific Instruments,* vol. 74, pp. 2918-2924, 2003.

[37] E. Furukawa, M. Mizuno, and T. Doi, "Development of a Flexure-Hinged Translation Mechanism Driven by Two Piezoelectric Stacks," *JSME International Journal,* vol. 38, pp. 743-748, 1995.

[38] T. King and W. Xu, "The Design and Characteristics of Piezomotors using Flexure-Hinged Displacement Amplifiers," *Robotics and Autonomous Systems,* vol. 19, pp. 189-197, 1996.

[39] K. R. Oldham, J. S. Pulskamp, R. G. Polcawich, and M. Dubey, "Thin-Film PZT Lateral Actuators With Extended Stroke," *Journal of Microelectromechanical Systems*, vol. 17, pp. 890-899, 2008.

[40] M. Muraoka and S. Sanada, "Displacement Amplifier for Piezoelectric Actuator based on Honeycomb Link Mechanism," *Sensors and Actuators A: Physical,* vol. 157, pp. 84-90, 2010.

[41] J. Ma, Y. Hu, B. Li, Z. Feng, and J. Chu, "Influence of Secondary Converse Piezoelectric Effect on Deflection of Fully Covered PZT Actuators," *Sensors and Actuators A: Physical,* vol. 175, pp. 132-138, 2012.

[42] G. Peng, Y. Kui, T. Xiaosong, X. He, S. Shannigrahi and L. Yaolong, "A Piezoelectric Micro-Actuator with Three Dimensional Structure and its Micro-Fabrication," in *Solid-State Sensors, Actuators and Microsystems*, vol. 10, pp. 713-716, 2005.

[43] Y. Sugawara, K. Onitsuka, S. Yoshikawa, Q. Xu, R. E. Newnham, and K. Uchino, "Metal–Ceramic Composite Actuators," *Journal of the American Ceramic Society,* vol. 75, pp. 996-998, 1992.

[44] M. Shikida, K. Sato, K. Takeshita, and S. Suzuki, "Response Time Measurement of Electrostatic S- Shaped Film Actuator Related to Environmental Gas Pressure Conditions," *An Investigation of Micro Structures, Sensors, Actuators, Machines and Systems*, pp. 210-215, 1996.

[45] A. B. Yu, X. M. Zhang, H. Cai, Q. X. Zhang, and A. Q. Liu, "Rhombic-Shaped Thermal Actuator Array for Evenly-Distributed Very Large Displacement," *IEEE International Conference on Micro Electro Mechanical Systems*, 2007.

[46] J. H. Comtois, and V. M. Bright, "Applications for Surface-Micromachined Polysilicon Thermal Actuators and Arrays," *Sensors and Actuators A: Physical,* vol. 58, pp. 19-25, 1997.

[47] G. Kovacs, L. Düring, S. Michel, and G. Terrasi, "Stacked Dielectric Elastomer Actuator for Tensile Force Transmission," *Sensors and Actuators A: Physical,* vol. 155, pp. 299-307, 2009.

[48] J. Tichy, J. Erhart, E. Kittinger, and J. Privratska, Fundamentals of Piezoelectric Sensorics Mechanical, Dielectric, and Thermodynamical Properties of Piezoelectric Materials. New York: Springer, 2010.

[49] K. C. Kao, Dielectric Phenomenon in Solids With Emphasis on Physical Concepts of Electronic Processes. Canada: Academic Press, 2004.

[50] B. Jaffe, W. R. Cook and H. Jaffe, "Piezoelectric Ceramics," Academic Press London, 1971.

[51] U. Kenji, "Advanced Piezoelectric Materials Science and Technology," Cambridge: Woodhead Publishing Limited, 2010.

[52] K. Heiji, "The Piezoelectricity of Poly (vinylidene Fluoride)," *Japanese Journal of Applied Physics,* vol. 8, pp. 975, 1969.

[53] E. Fukada and T. Furukawa, "Piezoelectricity and Ferroelectricity in Polyvinylidene Fluoride," *Ultrasonics,* vol. 19, pp. 31-39, 1981.

[54] E. D. Mason, "Manufacturing of Poly(vinylidene fluoride) and Evaluation of its Mechanical Properties," Master of Science, Materials Science and Engineering, Virginia Tech, 2002.

[55] "Piezo Systems Catalog,".

[56] "Measurement Specialties Catalog,".

[57] T. R. Jow and P. J. Cygan, "Investigation of Dielectric Breakdown of Polyvinylidene Fluoride using AC and DC methods," in *IEEE International Symposium on Electrical Insulation*, 1992, pp. 181-184.

[58] R. A. Wolf and S. T. McKinstry, "Temperature Dependence of the Piezoelectric Response in Lead Zirconate Titanate Films," *Journal of Applied Physics,* vol. 95, pp. 1397-1406, 2004.

[59] A. Vinogradov and F. Holloway, "Electro-Mechanical Properties of the Piezoelectric Polymer PVDF," *Ferroelectrics,* vol. 226, pp. 169-181, 1999.

[60] K. Wasa, T. Matsushima, H. Adachi, I. Kanno, and H. Kotera, "Thin-Film Piezoelectric Materials For a Better Energy Harvesting MEMS," *Journal of Microelectromechanical Systems*, vol. 21, pp. 451-457, 2012.

[61] O. D. Kwon, J. S. Yoo, Y. J. Yun, J. S. Lee, S. H. Kang, and K. J. Lim, "A Research on the Piezoelectric Vibration Actuator for Mobile Phone," *Electrical Insulating Materials*, vol. 3, pp. 676-678, 2005.

[62] Y. Sangduk, J. Kichang, C. Sanghyun, L. Yeonjung, K. Ohjo and K. Kyougsoo, "A Piezoelectric Actuator Driver Circuit for Automatic Focusing of Mobile Phone Cameras," *IEEE International Symposium on Circuits and Systems*, pp. 2106-2109, 2008.

[63] M. Schiffer, E. Obermeier, C. Stefanini, V. Manente, and P. Tunestal, "Low Power Piezoelectric Micro Mass Flow Controller for Liquid Fuel Injection," *Sensors*, pp. 1392-1395, 2007.

[64] J. Nuffer and T. Bein, "Application of Piezoelectric Materials in Transportation Industry," *Global Symposium on Innovative Solutions for the Advancement of the Transport Industry*, 2006.

[65] Y. Jiashi, "An Introduction to the Theory of Piezoelectricity," Springer Science and Business Media, 2005.

[66] J. Cheng, C. Liu, S. Shang, D. Liu, W. Perrie and G. Dearden, "A Review of Ultrafast Laser Materials Micromachining," *Optics and Laser Technology,* vol. 46, pp. 88-102, 2013.

[67] D. F. Berdy, P. Srisungsitthisunti, J. Byunghoo, X. Xianfan, J. F. Rhoads, and D. Peroulis, "Low-Frequency Meandering Piezoelectric Vibration Energy Harvester," *IEEE Transactions on Ultrasonics Ferroelectrics and Frequency Control*, vol. 59, pp. 846-858, 2012.

[68] A. N. Samant and N. B. Dahotre, "Laser Machining of Structural Ceramics—A Review," *Journal of the European Ceramic Society,* vol. 29, pp. 969-993, 2009.

[69] P. Srisungsitthisunti, O. K. Ersoy, and X. Xu, "Volume Fresnel Zone Plates Fabricated by Femtosecond Laser Direct Writing," *Applied Physics Letters,* vol. 90, 2007.

[70] S. Lee, E. V. Bordatchev, and M. J. F. Zeman, "Femtosecond Laser Micromachining of Polyvinylidene Fluoride (PVDF) Based Piezo Films," *Journal of Micromechanics and Microengineering,* vol. 18, pp. 1-8, 2008.

[71] H. Kim, V. Bedekar, R. A. Islam, L. W. Ho, D. Leo, and S. Priya, "Laser-Machined Piezoelectric Cantilevers for Mechanical Energy Harvesting," *IEEE Transactions on Ultrasonics, Ferroelectrics and Frequency Control*, vol. 55, pp. 1900-1905, 2008.

[72] D. W. Zeng, K. Li, K. C. Yung, H. L. W. Chan, C. L. Choy, and C. S. Xie, "UV Laser Micromachining of Piezoelectric Ceramic using a Pulsed Nd:YAG Laser," *Applied Physics,* vol. 78, pp. 415-421, 2004.

[73] E. A. Crum, "The Fountain Pen: A Collector's Companion," Philadelphia: Running Press, 1997.

[74] R. D. Piner, J. Zhu, F. Xu, S. Hong, and C. A. Mirkin, ""Dip-Pen" Nanolithography," *Science,* vol. 283, pp. 661-663, 1999.

[75] D. S. Ginger, H. Zhang, and C. A. Mirkin, "The Evolution of Dip-Pen Nanolithography," *Chemical International Edition,* vol. 43, pp. 30-45, 2004.

[76] K. Salaita, Y. Wang, and C. A. Mirkin, "Applications of Dip-Pen Nanolithography," *Nature Nanotechnology,* vol. 2, pp. 145-155, 2007.

[77] J. L. Wilbur, H. A. Biebuyck, J. C. MacDonald, and G. M. Whitesides, "Scanning Force Microscopies can Image Patterned Self-Assembled Monolayers," *Langmuir,* vol. 11, pp. 825-831, 1995.

[78] B. W. Maynor, S. F. Filocamo, M. W. Grinstaff, and J. Liu, "Direct-Writing of Polymer Nanostructures: Poly(thiophene) Nanowires on Semiconducting and Insulating Surfaces," *Journal of the American Chemical Society,* vol. 124, pp. 522-523, 2001.

[79] B. W. Maynor, Y. Li, and J. Liu, "Au “Ink” for AFM “Dip-Pen” Nanolithography," *Langmuir,* vol. 17, pp. 2575-2578, 2001.

[80] K. B. Lee, E. Y. Kim, C. A. Mirkin, and S. M. Wolinsky, "The Use of Nanoarrays for Highly Sensitive and Selective Detection of Human Immunodeficiency Virus Type 1 in Plasma," *Nano Letters,* vol. 4, pp. 1869-1872, 2004.

[81] D. C. Coffey and D. S. Ginger, "Patterning Phase Separation in Polymer Films with Dip-Pen Nanolithography," *Journal of the American Chemical Society,* vol. 127, pp. 4564-4565, 2005.

[82] P. E. Sheehan, L. J. Whitman, W. P. King, and B. A. Nelson, "Nanoscale Deposition of Solid Inks via Thermal Dip Pen Nanolithography," *Applied Physics Letters,* vol. 85, pp. 1589-1591, 2004.

[83] Y. Cai and B. M. Ocko, "Electro Pen Nanolithography," *Journal of the American Chemical Society,* vol. 127, pp. 16287-16291, 2005.

[84] X. Wang, K. S. Ryu, D. A. Bullen, J. Zou, H. Zhang and C. A. Mirkin, "Scanning Probe Contact Printing," *Langmuir,* vol. 19, pp. 8951-8955, 2003.

[85] H. Zhang, R. Elghanian, N. A. Amro, S. Disawal, and R. Eby, "Dip Pen Nanolithography Stamp Tip," *Nano Letters,* vol. 4, pp. 1649-1655, 2004.

[86] J. Zou, X. Wang, D. Bullen, K. Ryu, C. Liu, and A. M. Chad, "A Mould-and-Transfer Technology for Fabricating Scanning Probe Microscopy Probes," *Journal of Micromechanics and Microengineering,* vol. 14, pp. 204-211, 2004.

[87] K. H. Kim, N. Moldovan, and H. D. Espinosa, "A Nanofountain Probe with Sub-100nm Molecular Writing Resolution," *Small,* vol. 1, pp. 632-635, 2005.

VITA

VITA

Aarti Chigullapalli received her Bachelor of Engineering (B. E.) in Mechanical Engineering from Osmania University, Hyderabad, AP, India in June 2009 and her Ph.D. in Mechanical Engineering from Purdue University, West Lafayette, IN, in December 2014. Her research is focused on modeling and validation of nestable piezoelectric actuators.

List of Publications

[1] A. Chigullapalli, M. Sinani, Z. Luo, X. Xu, D. Peroulis and J. V. Clark , "Modeling and Validation of S-Drive: A Nestable Piezoelectric Actuator", to be submitted to *Sensors and Actuators: A Physical 2014*.
[2] A. Chigullapalli, and J. V. Clark , "Extremely Large Deflection Actuators for Translation or Rotation", *IMECE*, 2012, Houston, TX, USA.
[3] A. Chigullapalli, and J. V. Clark , "Towards Measuring Young's Modulus by Electronic Probing", *IMECE*, 2012, Houston, TX, USA.
[4] A. Chigullapalli, and J. V. Clark , "Towards Self-Calibratable MEMS Absolute Temperature Sensor: A Theoretical Study", *IMECE*, 2012.
[5] A. Chigullapalli, and J. V. Clark , "A Compact Flexure Model that Includes Fillets", *IMECE*, 2012, Houston, TX, USA.
[6] A. Chigullapalli, and J. V. Clark , "Modeling the Thermomechanical Interaction between an Atomic Force Microscope Cantilever and Laser Light", *IMECE*, 2012, Houston, TX, USA.
[7] A. Chigullapalli, and J. V. Clark , "Electro-Thermo-Mechanical beam Model", *Nanotech*, 2012, San Jose, CA, USA.
[8] A. Chigullapalli, and J. V. Clark ,"Measuring System Mass and Material Density of MEMS by Measuring Capacitance and Resonant Frequency: Simulated Experiment", *Nanotech*, 2012, San Jose, CA, USA.

[9] S.R. Mathur, A. Chigullapalli, and J. Murthy, "Benchmarking of Discrete Stochastic Galerkin Solver for Computational Fluid Dynamics", *SIAM CSE* 2011, Reno, Nevada.

[10] S.R. Mathur, A. Chigullapalli, and J. Murthy, *"*A Unified Unintrusive Discrete Approach to Sensitivity Analysis and Uncertainty Propagation in Fluid Flow Simulations*", IMECE,* 2010.